J. Mech. Phys. Solids 181 (2023) 105427

Contents lists available at ScienceDirect

Journal of the Mechanics and Physics of Solids

journal homepage: www.elsevier.com/locate/jmps

A Darcy–Cahn–Hilliard model of multiphase fluid-driven fracture

Alexandre Guével [a], Yue Meng [b], Christian Peco [c], Ruben Juanes [d], John E. Dolbow [a,*]

[a] *Department of Mechanical Engineering and Materials, Duke University, Durham, 27708, NC, USA*
[b] *Department of Geophysics, Stanford University, Stanford, 94305, CA, USA*
[c] *Department of Engineering Science and Mechanics, Penn State University, State College, 16801, PA, USA*
[d] *Department of Civil and Environmental Engineering, Massachusetts Institute of Technology, Cambridge, 02139, MA, USA*

ARTICLE INFO

Keywords:
Multiphase flow
Hydraulic fracturing
Phase-field
Porous media

ABSTRACT

A Darcy–Cahn–Hilliard model coupled with damage is developed to describe multiphase-flow and fluid-driven fracturing in porous media. The model is motivated by recent experimental observations in Hele–Shaw cells of the fluid-driven fracturing of a synthetic porous medium with tunable fracture resistance. The model is derived from continuum thermodynamics and employs several simplifying assumptions, such as linear poroelasticity and viscous-dominated flow. Two distinct phase fields are used to regularize the interface between an invading and a defending fluid, as well as the ensuing damage. The damage model is a cohesive version of a phase-field model for fracture, in which model parameters allow for control over both nucleation and crack growth. Simulations with finite elements are then performed to calibrate the model against recent experimental results. In particular, an experimentally-inferred phase diagram differentiating two flow regimes of porous invasion and fracturing is recovered. Finally, the model is employed to explore the parameter space beyond experimental capabilities, giving rise to the construction of an expanded phase diagram that suggests a new flow regime.

1. Introduction

The past few decades have witnessed an increased focus on obtaining a better understanding of multiphase flow in deformable porous media. This interest is driven by the prevalence of such phenomena in both natural and engineered systems, including enhanced geothermal energy, geological carbon storage, and geo-hazards (Juanes et al., 2020). Models that account for various aspects of the process can be extremely useful, as bench-scale experiments that mimic a wide range of subsurface conditions have proven to be elusive (Pyrak-Nolte et al., 2015). From a modeling standpoint, this class of problems is nonetheless challenging, with difficulties stemming from a three-way coupling between poromechanics, fracture mechanics, and multiphase fluid flow. This work introduces a novel double phase-field model in which both the fluid–fluid interface and the fracture surfaces are regularized and distinct. This permits the use of the model to explore a wide range of processes, including hydraulic fracturing, viscous fingering, and their combination. The model is developed within a simplified setting, hinging on linear poroelasticity and restricted to viscous flows. This paves the way for direct comparison with recent experiments examining multiphase-flow driven fracturing (Meng et al., 2020, 2022a, 2023). Beyond its ability to explain these recent observations, the broad potential of the model is utilized to build phase diagrams indicating both existing and new flow regimes.

The current model builds on a considerable amount of previous theoretical developments in which aspects of the underlying physics were examined in isolation or with some degree of coupling. This includes work on multiphase flow in rigid porous media,

---

* Corresponding author.
E-mail address: john.dolbow@duke.edu (J.E. Dolbow).

https://doi.org/10.1016/j.jmps.2023.105427
Received 26 May 2023; Received in revised form 28 August 2023; Accepted 30 August 2023

regularized models of fracture, and coupled poromechanics and fracture. In what follows, important theoretical works and recent modeling approaches that informed the current approach are discussed.

To begin with, the topic of multiphase flow in rigid porous media is one with a rich history. Here, emphasis is placed on the seminal work of Saffman and Taylor (1958), who studied the fluid–fluid displacement instability that occurs when an invading fluid is less viscous than the defending fluid. This phenomena has since become known as the viscous fingering instability. Subsequently, Lenormand et al. (1988) identified some of the conditions for viscous fingering, capillary fingering, and stable invasion to occur. More recently, Zhao et al. (2016) have augmented the parameter space of consideration by taking into account the role of wettability in multiphase flow. For a discussion of other important efforts in modeling multiphase flow through rigid porous media, the reader is referred to the recent paper by Juanes et al. (2020).

The modeling of multiphase flow often gravitates around a Cahn–Hilliard (Cahn and Hilliard, 1958) description of the interface between the fluids (Anderson et al., 1998; Kim, 2012). Such a regularization circumvents a shortcoming of sharp-interface approaches when it comes to modeling large interfacial deformation (Anderson et al., 1998), and, in particular, interfacial instabilities. Indeed, sharp-interface models break down when the interfacial thickness is comparable to the length scales of interest; this is often the case for interfacial instabilities (Anderson et al., 1998). The associated general description of multiphase flow led to the Navier–Stokes–Cahn–Hilliard model, introduced by Lowengrub and Truskinovsky (1998), which led to the Hele–Shaw–Cahn–Hilliard model (Lee et al., 2002) in the case of viscous flow in Hele–Shaw cells. The latter was proven to asymptotically converge to the corresponding Hele–Shaw sharp interface problem (Lee et al., 2002). The Navier–Stokes–Cahn–Hilliard model was later formally derived from a continuum thermodynamic framework by Abels et al. (2012). To do so, they took inspiration from Gurtin et al.'s work (Gurtin et al., 1995), formally deriving from the laws of thermodynamics the previously ad-hoc Navier–Stokes–Cahn–Hilliard models. In Lowengrub and Truskinovsky's derivation (Lowengrub and Truskinovsky, 1998), the binary fluid velocity was mass-averaged and not divergence-free, whereas in Abels et al.'s derivation (Abels et al., 2012), the velocity was volume-averaged and, advantageously, divergence-free. Dede et al. (2018) obtained the Hele–Shaw counterpart to the model of Abels et al. (2012), along with the proof of sharp interface convergence. Papatzacos (2002), Cueto-Felgueroso and Juanes (2008, 2009), and others, have applied such Cahn–Hilliard approaches to multiphase flow through porous media.

The potential for porous media to fracture complicates modeling efforts considerably due to the coupling between fluid flow and fracturing process. In essence, fluid pressure can drive the formation of new fracture surfaces, and the fracture openings, in turn, provide preferential paths for fluid flow. Most of the existing modeling efforts in this area have focused on hydraulic fracture and have been limited to instances in which the media is saturated with only one fluid, as opposed to multiphase flow. We refer the reader to the paper of Chen et al. (2021) for a recent review of models for hydraulic fracture.

More recently, advances in fracture mechanics have driven new developments in hydraulic fracture modeling. We focus in particular on models based on the variational treatment of fracture and accompanying phase-field regularizations (Francfort and Marigo, 1998; Bourdin et al., 2000). Early efforts to extend the basic phase-field approach for modeling fracture to coupling with fluid flow and hydraulic fracture were spearheaded by Miehe and collaborators (Miehe et al., 2015; Miehe and Mauthe, 2016). Their approach was based on Biot's (Biot, 1941) and Coussy's (Coussy, 2004) poromechanics framework cast in a variational formulation. This model opened avenues for embedding the well-established phase-field fracture approach into poromechanics. In particular, it proposed modifying the permeability to account for the flow enhancement due to fracturing. An alternative approach was derived from the Theory of Porous Media (Bowen, 1980; De Boer, 2012; Ehlers, 2002), which is the counterpart of Biot's empirical theory (Biot, 1941) embedded in continuum thermodynamics and the theory of mixtures (Truesdell and Toupin, 1960; Bowen, 1976). We refer in particular to the models of Ehlers and Luo (2017) and Wilson and Landis (2016). The main advances consist of the use of a thermodynamically-consistent framework for the model derivation and constitutive assumptions that permit a transition from Darcy-type flow in the pores to Stokes-type flow within open fractures. For further references on phase-field models of hydraulic fracture, the reader is referred to a recent review by Heider (2021).

The full three-way coupling of multiphase flow, poromechanics, and fracture has been investigated to a lesser extent, with some notable recent advances. For instance, Holtzman et al. (2012) experimentally identified, for non-cohesive granular media, the fracturing, capillary fingering, and viscous fingering regimes in a phase diagram representing fracturing number versus capillary number. On the modeling side, Lee et al. (2018) introduced a hydraulic fracturing model for two-phase flows using fracture phase-field modeling and lubrication theory. In a similar vein, Heider and Sun (2020) recently proposed a multiphase hydraulic fracturing model for both capillary and viscous flow. However, neither the work of Lee et al. (2018) nor Heider and Sun (Heider and Sun, 2020) regularized the fluid–fluid interfaces. As a result, these models are limited in their ability to account for aspects of the interfacial fluid dynamics.

Aspects of the model in this manuscript share common features with the recent works of Carrillo and Bourg (2021), and Paulin et al. (2022), as described below. Carrillo and Bourg (2021) adopted a fluid mechanics approach, treating soft porous media as an intermediate state between solid and fluid, which was effectively modeled through visco-plastic rheology. The model of Carrillo and Bourg (2021) allows for a clear distinction between the pore and continuum scales due to volume-averaging upscaling, as well as between viscous and capillary effects. While the distinction between viscous and capillary effects was made in the non-fracturing regime in the experimental study of Holtzman et al. (2012), the work of Carrillo and Bourg (2021) focused on this distinction in the fracturing regime. The latter also identified a regime of non-invasive fracturing, where invasion only occurs in the cracks and not in the porous medium. The model of Carrillo and Bourg (2021) relies on a local yield stress criterion to govern fracture and is limited in its ability to examine the potentially important role of fracture mechanics in governing the response of the system. Such a local, stress-based criterion for fracture is also likely to suffer from the kinds of spurious strain localization effects that plague local damage models (see, e.g., Pijaudier-Cabot and Bažant (1987)). Finally, we note that much like the aforementioned three-way coupling models, the fluid–fluid interfaces are not regularized in the work of Carrillo and Bourg (2021).

Paulin et al. (2022) developed a model for non-cohesive soft porous media which accounts for regularized damage and finite-deformation kinematics. The novelty of their work lies in envisioning the solid, liquid, and gas as three distinct phases, whose interactions are governed by interfacial energies of Cahn–Hilliard type. Although the model was developed for non-cohesive media, it employed a phase-field for fracture regularization that prevents the transmission of traction across fully damaged surfaces. Distinct from many of the aforementioned works, the model of Paulin et al. (2022) does not insist that damage be irreversible, such that fracture healing can occur. As the model was developed within the framework of continuum thermodynamics, it is thermodynamically consistent.

The approach described in this manuscript incorporates aspects that are similar to some of the aforementioned literature, with several important distinctions that are motivated by an interest in explaining recent experiments of fluid-driven fracturing of cohesive media (Meng et al., 2023). The configuration consists of a monolayer of beads that are lightly cemented together and placed into a Hele–Shaw cell, and saturated with a viscous defending fluid. The injection of a far less viscous invading fluid into this system gives rise to a clear coupling between fracturing and fluid invasion in which the fracture resistance of the skeleton plays an important role in delineating various regimes of the response. In the configuration examined in this work, one can expect new features such as a non-trivial injection pressure curve and the possibility of viscous fingering instabilities. The former feature can be explained by the fact that both the solid's cement and the defending fluid's viscosity act as a resistance to fracture and invasion of the injected fluid.

Accordingly, for the fracture model, this work adopts a cohesive variation on the well-established phase-field regularization for fracture. In particular, the model described in Geelen et al. (2019) is used. It incorporates an energetic threshold for damage that is insensitive to the choice of regularization length. To accommodate fluid–fluid interface instabilities, a second phase field is employed, representing the invading fluid saturation. This allows merging the two-pronged effort described above, and, in particular, expanding the space of potential flow regimes. The aforementioned works have identified six different types of flow regimes: uniform invasion, capillary and viscous fingering, invasive capillary and viscous fracturing, and non-invasive fracturing. A supplementary decomposition could be made between cohesive and non-cohesive fracturing. In this contribution, a new regime where viscous fracturing and viscous fingering are combined is revealed. For that, and in line with the experiments of Meng et al. (2023), attention is confined to viscous flows (large capillary numbers), leaving aside the capillary regimes.

This manuscript is divided into three main sections: (1) a description of the aforementioned Hele–Shaw experiments; (2) a theoretical derivation of the model; and (3) results from simulations that explore the capabilities and predictions of the model. First, the experimental setup and the key observations and measurements of Meng et al. (2023) are summarized. The modeling strategy is then described, yielding a Darcy–Cahn–Hilliard model of fluid-driven fracture with multiphase flow. The composite model is assembled through a continuum thermodynamic derivation to ensure a consistent coupling of the different components. Namely, these components are inspired from Gurtin et al. (1995) and Cogswell and Szulczewski (2017) for the multiphase flow, and from Ehlers (Ehlers, 2002; Ehlers and Luo, 2017) and Borja (2006) for poromechanics. The novelty in the fracture modeling will be to employ a cohesive fracture model (Geelen et al., 2019; Hu et al., 2020, 2021) which allows for controlling both the onset of cracks and their propagation, but also accounts for rate effects through a damage viscosity. The resulting system of coupled partial differential equations is discretized using the finite-element method. Simulations are then employed to calibrate various parameters against the experimental observations, and to reproduce a phase diagram representing modified capillary number versus cement volume ratio. Finally, the parameter space to build a new phase diagram that extends beyond the experimental observations is explored, yielding a new dimensionless group of interest and a new type of flow regime mixing fracturing and viscous fingering.

2. Description of recent experiments

In this section, recent experiments conducted at MIT concerning the fluid-driven fracturing of a cemented pack of beads in a Hele–Shaw cell (Meng et al., 2022b, 2023) are briefly described. Observations from these experiments are employed to motivate simplifying assumptions in the model's derivation. Subsequently, they are used to both calibrate various parameters in the model and demonstrate some of its capabilities and limitations.

The experimental configuration consists of a monolayer of spherical beads that are cemented together. Both the beads and cement are made from polyurethane rubber, which enables the use of photoporoelasticity, a technique developed by Li et al. (2021) to visualize the effective stress field. The amount of cement can be controlled, effectively modulating the fracture resistance of the skeleton. The skeleton is placed between the two plates of the Hele–Shaw cell, and the plates are held at a constant distance from each other with four outer clamps. The system is then saturated with oil and water is injected at the center. As such, the entire system effectively approximates a deformable porous media interacting with multiphase flow. Aspects of the experimental setup are very similar to those conducted for non-cohesive granular media, as described in Meng et al. (2022a).

In the most recent experiments (Meng et al., 2023), the cement renders the granular media cohesive, with the degree of cohesion effectively delineating two regimes in the response of the system. For sufficiently high cement volume fractions, the solid skeleton deforms but does not fracture as the water invades the media and expels the defending oil. Conversely, as the amount of cement is decreased, the fracture resistance of the solid skeleton also decreases, and at some point the forces on the skeleton are sufficiently large to break the cement bonds and permit fracture patterns to emerge.

The values of the main parameters are listed in Table B.1. Note in particular the oil viscosity η_o, which is five orders of magnitude larger than the water viscosity η_w. This gives rise to a relatively large viscous pressure drop δp_{vis} (see (50)), acting as a driving force responsible for fracturing the cemented beads. The high contrast in fluid viscosities was necessary to compensate for the limited injection rate delivered by the laboratory pump.

Another aspect of the type of experiment focused on in this work, in contrast to more conventional settings with low-permeability porous media, is the fact that the invading fluid can leak off the fracture: the water flows both in the opening fractures and in the pore spaces of the undamaged domain. Following the description by Carrillo and Bourg (2021), this type of response is referred to as "invasive fracturing". A last feature of interest is that the injection pressure keeps increasing as the cracks form, almost until the water reaches the edge of the cell. This is expected to be the case as long as cracks are continuing to grow (see, e.g., Figure 7 in Santillán et al. (2018)), which is the case in the experiments and in the corresponding simulations.

It bears emphasis that the mechanical and fracture response of the cement-bead network was experimentally characterized independently in dry conditions. The experimentally measured bulk moduli are listed in Table B.1. As for the fracture toughness, the critical mode-I stress intensity factor K_{1c} was measured via a dog-bone tension test. As a function of the cement ratio C (expressed in %), it was experimentally found that $K_{1c} = 0.15\mathrm{C} + 0.59\,\mathrm{kPa\,m}^{1/2}$, so that

$$G_c = \frac{K_{1c}(C)^2}{E/(1-\nu^2)}. \tag{1}$$

This assumes brittle failure, which is confirmed by the stress–strain output of the tensile test showing a linear increase of the stress until failure, followed by a sharp decrease; that is, there is negligible plastic deformation and ductile failure can be neglected.

3. Derivation

3.1. *Overall framework and approach*

The model uses two distinct phase fields to regularize geometric features of interest (see Fig. 1). The first phase field, denoted by S, corresponds to the invading fluid saturation, so that $S = 1$ in the invading fluid and $S = 0$ in the defending fluid. Intermediate values of S correspond to the diffuse interface, of thickness l_S, which regularizes the otherwise sharp interface and ensures a smooth transition from 0 to 1. The second phase field d can be similarly described in that it discriminates between fully cracked regions, where $d = 1$, and fully intact regions, where $d = 0$. The thickness of the damage band is characterized by the regularization length l_d.

Although the resulting phase-field equations will end up looking similar, the saturation phase-field stems from a gradient energy regularization, following the pioneering work of Cahn (Cahn and Hilliard, 1958), whereas the damage phase-field theory stems from a variational regularization of Griffith's crack surface energy, as introduced by Francfort and Marigo (1998). Both phase-field approaches are reconciled by the configurational theory of Fried and Gurtin (1994), Gurtin (1996), da Silva et al. (2013), whereby phase-field equations are derived from a fundamental law, the micro-force balance. The latter approach is followed in this work to derive the evolution equations governing both phase fields.

3.2. *Notation and terminology*

Consider a porous medium consisting of three components: one solid and two pore fluids. In keeping with Coussy's theory and terminology (Coussy, 2004) (see section 1.1 therein), a porous medium is modeled as the superimposition of a solid *skeleton* continuum (formed by the solid *matrix* and the connected pore space emptied of fluid) and of a pore-filling (binary) fluid continuum. Both subscripts and superscripts will be used to denote fields associated with one of the components. In particular, s is used to denote the solid component and $\alpha = \{1,2\}$ is used to denote the fluid components, with $\alpha = 1$ representing the invading fluid and $\alpha = 2$ the defending fluid.

The true volume fractions of the components are denoted by ϕ^s, ϕ^1, and ϕ^2, and satisfy $\phi^s + \phi^1 + \phi^2 = 1$. They measure the volume of each phase per unit current bulk volume. Therefore, $\phi = \phi^1 + \phi^2$ measures the volume of pores per unit current bulk volume. Similarly, the respective partial densities (at the macroscale, or continuum scale) are denoted by ρ^s and ρ^α, and the partial Cauchy stresses by $\boldsymbol{\sigma}^s$ and $\boldsymbol{\sigma}^\alpha$. The corresponding intrinsic quantities (at the mesoscale, or pore scale) are denoted with subscripts. The volume fraction of each fluid in the pores is described by the saturations S^α, whereby $S^1 + S^2 = 1$.

Given the above notations, some key relationships can be summarized as:

$$\begin{aligned}
&\phi^s = 1-\phi, &&\phi^\alpha = \phi S^\alpha, &&\phi = \phi^1 + \phi^2,\\
&\rho^s = (1-\phi)\rho_s, &&\rho^\alpha = \phi S^\alpha \rho_\alpha, &&\rho^f = \rho^1 + \rho^2,\\
&\boldsymbol{\sigma}^s = (1-\phi)\boldsymbol{\sigma}_s, &&\boldsymbol{\sigma}^\alpha = \phi S^\alpha \boldsymbol{\sigma}_\alpha, &&\boldsymbol{\sigma}^f = \boldsymbol{\sigma}^1 + \boldsymbol{\sigma}^2,
\end{aligned} \tag{2}$$

where tensorial quantities are written in bold font. In (2), the three columns are associated with the solid phase, the individual fluid phases, and the resulting binary fluid, respectively.

Finally, let $\boldsymbol{x}$ denote the coordinate vectors in the current configuration. Upon noting a a general scalar quantity, $\boldsymbol{a}$ a general vector, $\boldsymbol{A}$ and $\boldsymbol{B}$ two general tensors, and adopting the Einstein summation convention, the following conventions for the spatial gradient, spatial divergence, and double contraction are employed in the following: $(\nabla a)_i = \frac{\partial a}{\partial x_i}$, $(\nabla \boldsymbol{a})_{ij} = \frac{\partial a_i}{\partial x_j}$, $\nabla \cdot \boldsymbol{a} = \frac{\partial a_i}{\partial x_i}$, $(\nabla \cdot \boldsymbol{A})_i = \frac{\partial A_{ij}}{\partial x_j}$, $\boldsymbol{A} : \boldsymbol{B} = A_{ij}B_{ij}$.

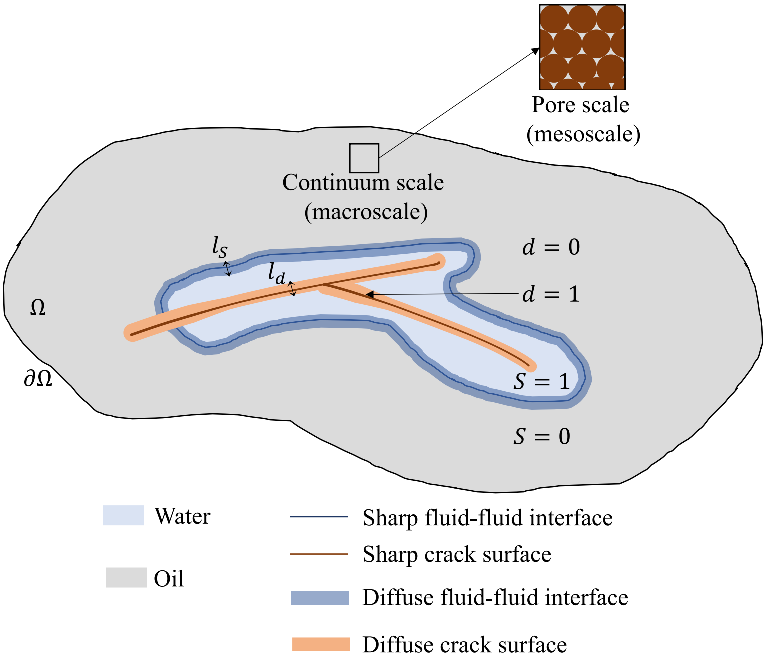

Fig. 1. Schematic of the modeling of the fluid–fluid interface and crack surfaces through the phase fields S (water saturation) and d (damage), respectively.

3.3. Main assumptions

Consider the isothermal motion of a binary fluid through a deformable porous skeleton, and assume that the two components of the binary fluid are incompressible (i.e. ρ_1 and ρ_2 are constant) and immiscible. The reader is referred to Lowengrub and Truskinovsky's derivation (Lowengrub and Truskinovsky, 1998) when fluids are compressible or quasi-incompressible. For simplicity, and consistent with the experiments described in Section 2, further assume that the difference in densities ρ_1 and ρ_2 is negligible. The reader is referred to Abels et al. (2012) for a derivation when this assumption does not hold. Following Gurtin et al. (1995), also assume that "the momenta and kinetic energies of the constituents are negligible when computed relative to the gross motion of the fluid". This means in particular that the binary fluid is tracked in time through the material time derivative associated with the average velocity

$$\boldsymbol{v}_f = S\boldsymbol{v}_1 + (1 - S)\boldsymbol{v}_2. \tag{3}$$

Furthermore, assume that the capillary number (the ratio of viscous forces to capillary forces, see $(49)_2$) is sufficiently high such that the pore pressure p is identical in both phases 1 and 2, and also that the flow is sufficiently slow to neglect the fluid's kinetic energy. In other words, consider a viscous flow. In the case where capillary effects cannot be neglected (low capillary number), the effect of the mean pore pressure p should be decomposed into the separate effects of the pressures of both phases. The reader is referred to the derivation of Ehlers (2018) following the Theory of Porous Media, and to the work of Cueto-Felgueroso and Juanes (2014) and Paulin et al. (2022) for an alternative approach.

With regard to the porous skeleton, small deformations are assumed, so that the formulation falls in the framework of linear poroelasticity. Unlike the fluid components, the solid matrix is assumed to be compressible, so that its density is not constant. This assumption is justified by the fact that, in the experiments described in Section 2, the beads comprising the porous medium have a bulk modulus that is three orders of magnitude smaller than that of water. The resulting continuum is approached through the Theory of Porous Media (see, e.g., Ehlers and Luo (2017) and Ehlers (2002)), that is, it stems from the superimposition of the continua formed by the different solid and fluid components.

3.4. Mass balance

To derive the mass balance equations for the three phases, the derivation here follows Coussy (2004), Borja (2006), and Ehlers (2002), Ehlers and Luo (2017), combined with Gurtin et al. (1995).

The partial fluxes associated with the fluid constituents 1 and 2 are denoted by $\tilde{\boldsymbol{h}}^1$ and $\tilde{\boldsymbol{h}}^2$, respectively. As these are internal to the fluid mixture, they satisfy $\tilde{\boldsymbol{h}}^1 + \tilde{\boldsymbol{h}}^2 = \boldsymbol{0}$. In what follows, a superposed dot is used to denote the material time derivative following the solid skeleton motion. The solid velocity $\boldsymbol{v}_s$ is therefore given by $\boldsymbol{v}_s = \dot{\boldsymbol{u}}_s$, where $\boldsymbol{u}_s$ denotes the solid displacement.

With these definitions in hand, the balances for the solid skeleton and the two fluid phases read

$$\begin{aligned}&\dot{\rho}^s + \rho^s \nabla \cdot \boldsymbol{v}_s = 0,\\ &\dot{\rho}^\alpha + \rho^\alpha \nabla \cdot \boldsymbol{v}_s + \nabla \cdot \rho_\alpha \boldsymbol{w}_\alpha = -\nabla \cdot \tilde{\boldsymbol{h}}^\alpha,\end{aligned} \tag{4}$$

where $\nabla = \partial/\partial \boldsymbol{x}$ denotes the spatial gradient, and $\boldsymbol{w}_\alpha = \phi^\alpha(\boldsymbol{v}_\alpha - \boldsymbol{v}_s)$ is the Darcy flux of phase α. Note that the right side of $(4)_1$ vanishes because there is no mass exchange between the solid phase and either of the liquid phases.

Following Borja's strategy (Borja, 2006), a one-to-one relationship is assumed to exist between the solid density ρ_s and the pore pressure p (barotropic flow). The corresponding functional relationship can be expressed as $\rho_s = \hat{\rho}_s(p)$. As a result, $\rho^s = (1-\phi)\rho_s = \hat{\rho}^s(\phi, p)$, or equivalently $p = \hat{p}(\phi, \rho^s)$. Following Borja (2006) (see Appendix A), these relationships lead to the following equivalent forms of the solid mass balance $(4)_1$, both of which will prove useful in the model's derivation:

$$\begin{aligned}&\dot{\overline{1-\phi}} + (1-\phi)\left(\nabla \cdot \boldsymbol{v}_s + \frac{\dot{p}}{K_s}\right) = 0,\\ &\dot{\overline{1-\phi}} + (b-\phi)\nabla \cdot \boldsymbol{v}_s = 0,\end{aligned} \tag{5}$$

where $b = 1 - K/K_s$ denotes Biot's coefficient, K_s is the bulk modulus of the matrix and K is the bulk modulus of the skeleton.[1] Both K and K_s are assumed to be constants in this work.

As for the mass balances of the incompressible fluid constituents, dividing $(4)_2$ by the constant densities yields

$$\begin{aligned}&\dot{\overline{\phi S_1}} + \phi S_1 \nabla \cdot \boldsymbol{v}_s + \nabla \cdot \boldsymbol{w}_1 = -\nabla \cdot \boldsymbol{h}^1,\\ &\dot{\overline{\phi S_2}} + \phi S_2 \nabla \cdot \boldsymbol{v}_s + \nabla \cdot \boldsymbol{w}_2 = -\nabla \cdot \boldsymbol{h}^2,\end{aligned} \tag{6}$$

where $\boldsymbol{h}^\alpha = \tilde{\boldsymbol{h}}^\alpha/\rho_\alpha$. Summing up the two previous equations, the mass balance of the binary fluid can be written as

$$\dot{\phi} + \phi \nabla \cdot \boldsymbol{v}_s + \nabla \cdot \boldsymbol{w} = 0, \tag{7}$$

where $\boldsymbol{w} = \boldsymbol{w}_1 + \boldsymbol{w}_2 = \phi \boldsymbol{v}_{f/s}$ is the Darcy flux of the binary fluid and $\boldsymbol{v}_{f/s} = S(\boldsymbol{v}_1 - \boldsymbol{v}_s) + (1-S)(\boldsymbol{v}_2 - \boldsymbol{v}_s)$, the velocity of the binary fluid with respect to the solid, is defined here for later use. Then, summing up the mass balances of the solid $(5)_2$ and of the binary fluid (7) yields the mass balance of the mixture:

$$b \nabla \cdot \boldsymbol{v}_s + \nabla \cdot \boldsymbol{w} = 0. \tag{8}$$

Finally, for later use, it will be helpful to have at hand some alternative expressions of the fluid mass balances. A superposed circle (e.g., $\overset{\circ}{a}$), is used to denote the material time derivative following the binary fluid, which travels at velocity $\boldsymbol{v}_f$ (3). The mass balances of each fluid component and of the resulting binary fluid can thus be rewritten as

$$\begin{aligned}&\overset{\circ}{\overline{\phi S_\alpha}} + \phi S_\alpha \nabla \cdot \boldsymbol{v}_f = -\nabla \cdot \boldsymbol{h}^\alpha,\\ &\overset{\circ}{\phi} + \phi \nabla \cdot \boldsymbol{v}_f = 0.\end{aligned} \tag{9}$$

3.5. Force balances

The macro-force balances of the solid and binary fluid read

$$\begin{aligned}&\nabla \cdot \boldsymbol{\sigma}^s + \boldsymbol{f}^{fs} = 0,\\ &\nabla \cdot \boldsymbol{\sigma}^f + \boldsymbol{f}^{sf} = 0,\end{aligned} \tag{10}$$

where $\boldsymbol{\sigma}^s$ and $\boldsymbol{\sigma}^f$ denote the partial solid and fluid Cauchy stresses, respectively, while $\boldsymbol{f}^{fs}$ and $\boldsymbol{f}^{sf}$ are the forces exerted by the fluid upon the solid and vice-versa. The effects of external body forces like gravity have been neglected. The forces satisfy the reciprocity relationship $\boldsymbol{f}^{fs} + \boldsymbol{f}^{sf} = 0$. They are also referred to as momentum productions in Ehlers and Luo's work (Ehlers and Luo, 2017). They result from the superimposition of the continua formed by the solid and the binary fluid.

The above form of the force balance for the binary fluid stems from neglecting the relative momenta of the constituents, as in Gurtin et al.'s derivation (Gurtin et al., 1995). In particular, recall that neglecting capillary effects, the pore pressure is assumed to be the same in both phases. As a result, the force balance for the mixture, described by the total stress $\boldsymbol{\sigma} = \boldsymbol{\sigma}^s + \boldsymbol{\sigma}^f$, reads

$$\nabla \cdot \boldsymbol{\sigma} = 0. \tag{11}$$

A derivation similar to that in Gurtin et al. (1995) would also show that the symmetry of $\boldsymbol{\sigma}^s$ and $\boldsymbol{\sigma}^f$ follows from the corresponding balances of angular momentum. The fluid stress tensor can be written in terms of its shear component $\boldsymbol{\tau}$ and the pore pressure p as $\boldsymbol{\sigma}^f = \phi(\boldsymbol{\tau} - p\boldsymbol{I})$.

---

[1] In this work, consistent with the work of Coussy (2004), the term "skeleton" denotes the continuum formed by the solid matrix and the connected pore space, emptied of fluid. With reference to the experiments described in Section 2, the skeleton consists of the aggregate comprised by the collection of beads, the cement and the empty pores, whereas the "matrix" consists solely of the bead material.

Finally, following the configurational theory of Fried and Gurtin (Fried and Gurtin, 1994; Gurtin, 1996), the phase fields S and d are governed by the following microforce balances:

$$\begin{aligned} &\nabla \cdot \xi_d + \pi_d = 0, \\ &\nabla \cdot \xi_S + \pi_S = 0, \end{aligned} \tag{12}$$

where ξ denotes the microstress that is energetically conjugate to the gradient of the respective phase field, and π the microforce that is conjugate to the phase field.

3.6. Dissipation inequality

Within the framework of continuum thermodynamics, constitutive restrictions for the governing equations are now invoked. In addition to the quantities introduced previously, the partial Helmholtz free energies per unit mass for the solid and binary fluid are denoted by ψ^s and ψ^f, respectively. The chemical potential of constituent α associated with the flux $\boldsymbol{h}^\alpha$ is denoted by μ_α. Since these fluxes are complementary, in this section attention is restricted to constituent 1 and $\boldsymbol{h}$ is used in place of $\boldsymbol{h}^1$ and μ is used to denote the difference in chemical potentials, i.e. $\mu = \mu_1 - \mu_2$ (see Gurtin et al. (1995)). Similarly, S is used in place of S_1.

The second law expressed in the form of the dissipation inequality requires that (see Gurtin et al. (1995)), for an arbitrary spatial region Ω_t of the mixture (in the current configuration), the rate at which the energy of Ω_t increases (following the Theory of Porous Media (Ehlers, 2002) and neglecting the kinetic energy),

$$\overset{\cdot}{\overline{\int_{\Omega_t} \rho^s \psi^s \, \mathrm{d}V}} + \overset{\circ}{\overline{\int_{\Omega_t} \rho^f \psi^f \, \mathrm{d}V}} \tag{13}$$

is limited by the external work on Ω_t,

$$\int_{\partial\Omega_t} \boldsymbol{\sigma}^s \boldsymbol{n} \cdot \dot{\boldsymbol{u}}_s \, \mathrm{d}A + \int_{\partial\Omega_t} \dot{d} \boldsymbol{\xi}_d \cdot \boldsymbol{n} \, \mathrm{d}A + \int_{\partial\Omega_t} \boldsymbol{\sigma}^f \boldsymbol{n} \cdot \boldsymbol{v}_f \, \mathrm{d}A + \int_{\partial\Omega_t} \overset{\circ}{S} \boldsymbol{\xi}_S \cdot \boldsymbol{n} \, \mathrm{d}A, \tag{14}$$

plus the rate at which energy is transported to Ω_t by diffusion (Gurtin et al., 1995),

$$-\int_{\partial\Omega_t} \mu_\alpha \boldsymbol{h}^\alpha \cdot n \, \mathrm{d}A = -\int_{\partial\Omega_t} \mu \boldsymbol{h} \cdot n \, \mathrm{d}A. \tag{15}$$

In the first line of the dissipation inequality (13), the Reynolds transport theorem yields:

$$\begin{aligned} \overset{\cdot}{\overline{\int_{\Omega_t} \rho^s \psi^s \, \mathrm{d}V}} &= \int_{\Omega_t} \left(\overset{\cdot}{\overline{\rho^s \psi^s}} + \rho^s \psi^s \nabla \cdot \boldsymbol{v}_s \right) \, \mathrm{d}V \\ &= \int_{\Omega_t} \left((\dot{\rho}^s + \rho^s \nabla \cdot \boldsymbol{v}_s) \psi^s + \rho^s \dot{\psi}^s \right) \, \mathrm{d}V \\ &= \int_{\Omega_t} \rho^s \dot{\psi}^s \, \mathrm{d}V, \end{aligned} \tag{16}$$

where the solid mass balance $(4)_1$ has applied. A similar result is obtained for the fluid energy term in (13).

In the second line of the dissipation inequality (14), the first and third terms are the mechanical power expended by the macroforces responsible for deforming the solid and binary fluid, respectively. The second and fourth terms are the mechanical power developed by the configurational microforces responsible for changes in the phase fields d and S, respectively.

For the third line, the reader is referred to the book by Gurtin et al. (2010) for a treatment of constituents transport through continuum thermodynamics (see part 12 therein).

Using the divergence theorem, the local form of the dissipation inequality is then obtained as follows:

$$\begin{aligned} \rho^s \dot{\psi}^s + \rho^f \overset{\circ}{\psi^f} \leq\; &\boldsymbol{\sigma}^s : \nabla \boldsymbol{v}_s + \boldsymbol{v}_s \cdot \nabla \cdot \boldsymbol{\sigma}^s + \boldsymbol{\xi}_d \cdot \nabla \dot{d} + \dot{d} \nabla \cdot \boldsymbol{\xi}_d + \boldsymbol{\sigma}^f : \nabla \boldsymbol{v}_f \\ &+ \boldsymbol{v}_f \cdot \nabla \cdot \boldsymbol{\sigma}^f + \boldsymbol{\xi}_S \cdot \nabla \overset{\circ}{S} + \overset{\circ}{S} \nabla \cdot \boldsymbol{\xi}_S - \mu \nabla \cdot \boldsymbol{h} - \boldsymbol{h} \cdot \nabla \mu. \end{aligned} \tag{17}$$

Using the force balances (10) and (12), and the mass balance of the invading fluid (9), one obtains

$$\begin{aligned} \rho^s \dot{\psi}^s + \rho^f \overset{\circ}{\psi^f} \leq\; &\boldsymbol{\sigma}^s : \nabla v_s - \boldsymbol{v}_s \cdot \boldsymbol{f}^{fs} + \boldsymbol{\xi}_d \cdot \nabla \dot{d} - \pi_d \dot{d} + \boldsymbol{\sigma}^f : \nabla \boldsymbol{v}_f \\ &- \boldsymbol{v}_f \cdot \boldsymbol{f}^{sf} + \boldsymbol{\xi}_S \cdot \nabla \overset{\circ}{S} - \pi_S \overset{\circ}{S} + \mu \phi \overset{\circ}{S} - \boldsymbol{h} \cdot \nabla \mu. \end{aligned} \tag{18}$$

In particular, the derivation uses the relationship $\phi \overset{\circ}{S} = -\nabla \cdot \boldsymbol{h}$, which can be obtained by multiplying $(9)_2$ by S and subtracting $(9)_1$ (particularized for fluid constituent 1) from it. The familiar poromechanical concept of effective stress can be obtained by adding the null term $(\boldsymbol{\sigma} - \boldsymbol{\sigma}^s - \boldsymbol{\sigma}^f) : \nabla \boldsymbol{v}_s$ to (18), yielding

$$\begin{aligned} \rho^s \dot{\psi}^s + \rho^f \overset{\circ}{\psi^f} \leq\; &\boldsymbol{\sigma} : \nabla \boldsymbol{v}_s + \boldsymbol{\xi}_d \cdot \nabla \dot{d} - \pi_d \dot{d} + \boldsymbol{\sigma}^f : \nabla \boldsymbol{v}_{f/s} \\ &- \boldsymbol{v}_{f/s} \cdot \boldsymbol{f}^{sf} + \boldsymbol{\xi}_S \cdot \nabla \overset{\circ}{S} + (\phi \mu - \pi_S) \overset{\circ}{S} - \boldsymbol{h} \cdot \nabla \mu. \end{aligned} \tag{19}$$

Following the derivation by Ehlers and Luo (2017), the pore pressure is then employed as a Lagrange multiplier, multiplying (8) by p and adding it to the previous inequality to obtain:

$$\begin{aligned} \rho^s \dot{\psi}^s + \rho^f \overset{\circ}{\psi^f} \leq \boldsymbol{\sigma}' : \nabla \boldsymbol{v}_s + \boldsymbol{\xi}_d \cdot \nabla \dot{d} - \pi_d \dot{d} + \phi \boldsymbol{\tau} : \nabla \boldsymbol{v}_{f/s} + p \boldsymbol{v}_{f/s} \cdot \nabla \phi \\ - \boldsymbol{v}_{f/s} \cdot \boldsymbol{f}^{sf} + \boldsymbol{\xi}_S \cdot \nabla \overset{\circ}{S} + (\phi \mu - \pi_S) \overset{\circ}{S} - \boldsymbol{h} \cdot \nabla \mu, \end{aligned} \tag{20}$$

where $\boldsymbol{\sigma}' = \boldsymbol{\sigma} + bp\boldsymbol{I}$ denotes the effective stress. The last step consists in identifying the energy-conjugates, which are the products of forces and rates of state variables. For that, one must carefully commute gradients and time derivatives, especially when the former are spatial quantities whereas the latter are material quantities, as here, in which case one must employ the following commutator identity (see e.g. Gurtin et al. (1995)):

$$\nabla \left(\frac{\mathrm{d}^\alpha \varphi}{\mathrm{d}t} \right) = \frac{\mathrm{d}^\alpha}{\mathrm{d}t} (\nabla \varphi) + (\nabla \boldsymbol{v}_\alpha)^T \nabla \varphi. \tag{21}$$

Thereupon,

$$\begin{aligned} \nabla \dot{d} &= \dot{\overline{\nabla d}} + (\nabla \boldsymbol{v}_s)^T \nabla d \approx \dot{\overline{\nabla d}}, \\ \nabla \dot{\boldsymbol{u}}_s &= \dot{\overline{\nabla \boldsymbol{u}_s}} + (\nabla \boldsymbol{v}_s)^T \nabla \boldsymbol{u}_s \approx \dot{\overline{\nabla \boldsymbol{u}_s}}, \\ \nabla \overset{\circ}{S} &= \overset{\circ}{\overline{\nabla S}} + (\nabla \boldsymbol{v}_f)^T \nabla S, \end{aligned} \tag{22}$$

where the approximations in the two first equations stem from the linear poroelasticity assumption that second-order terms in deformation are negligible (see e.g. section 3 in MacMinn et al. (2016)). In particular, assume that d varies like ϕ since their evolution is tightly coupled, as the simulations in this work will indicate. The local dissipation inequality (20) then reads:

$$\begin{aligned} \rho^s \dot{\psi}^s + \rho^f \overset{\circ}{\psi^f} \leq (\boldsymbol{\sigma}' + \nabla S \otimes \boldsymbol{\xi}_S) : \dot{\overline{\nabla \boldsymbol{u}_s}} + \boldsymbol{\xi}_d \cdot \dot{\overline{\nabla d}} - \pi_d \dot{d} \\ + (\phi \boldsymbol{\tau} + \nabla S \otimes \boldsymbol{\xi}_S) : \nabla \boldsymbol{v}_{f/s} + (p \nabla \phi - \boldsymbol{f}^{sf}) \cdot \boldsymbol{v}_{f/s} \\ + \boldsymbol{\xi}_S \cdot \overset{\circ}{\overline{\nabla S}} + (\phi \mu - \pi_S) \overset{\circ}{S} - \boldsymbol{h} \cdot \nabla \mu. \end{aligned} \tag{23}$$

The change of variable $\hat{\mu} = \phi \mu$ is applied and the hat notation is dropped thereafter for clarity. Identifying as state variables $\{\nabla \boldsymbol{u}_s, d, \nabla d, \dot{d}, \boldsymbol{v}_{f/s}, \boldsymbol{D}, S, \nabla S, \mu, \nabla \mu\}$, where $\boldsymbol{D} = (\nabla \boldsymbol{v}_{f/s} + \nabla \boldsymbol{v}_{f/s}{}^T)/2$ denotes the strain rate tensor for the binary fluid (Gurtin et al., 1995), and invoking Ehlers' principle of phase separation (Ehlers and Luo, 2017), consider the constitutive dependencies:

$$\begin{aligned} \psi^s &= \hat{\psi}^s(\nabla \boldsymbol{u}_s, d, \nabla d, \dot{d}) = \hat{\psi}^s(\dots)_s, \\ \psi^f &= \hat{\psi}^f(\boldsymbol{v}_{f/s}, \boldsymbol{D}, S, \nabla S, \mu, \nabla \mu) = \hat{\psi}^f(\dots)_f, \\ \boldsymbol{\sigma}' &= \hat{\boldsymbol{\sigma}}'(\dots)_s, \\ \boldsymbol{\xi}_d &= \hat{\boldsymbol{\xi}}_d(\dots)_s, \\ \pi_d &= \hat{\pi}_d(\dots)_s, \\ \boldsymbol{\tau} &= \hat{\boldsymbol{\tau}}(\dots)_f, \\ \boldsymbol{\xi}_S &= \hat{\boldsymbol{\xi}}_S(\dots)_f, \\ \pi_S &= \hat{\pi}_S(\dots)_f, \\ \boldsymbol{\tau} &= \hat{\boldsymbol{\tau}}(\dots)_f, \\ p &= \hat{p}(\dots)_f, \\ \boldsymbol{h} &= \hat{\boldsymbol{h}}(\dots)_f. \end{aligned} \tag{24}$$

In addition, from the barotropic flow assumption in Section 3.4 and the definition $\rho^f = \phi \rho_f$, where ρ_f is constant, the constitutive dependencies $\rho^s = \hat{\rho}^s(\phi, p)$ and $\rho^f = \hat{\rho}^f(\phi)$ hold. This hereby-defined constitutive model satisfies the dissipation inequality (23) if and only if

$$\begin{aligned} &\left(\hat{\boldsymbol{\sigma}}'(\dots)_s + \nabla S \otimes \hat{\boldsymbol{\xi}}_S(\dots)_f - \hat{\rho}^s \frac{\partial \hat{\psi}^s(\dots)_s}{\partial \nabla \boldsymbol{u}_s} \right) : \dot{\overline{\nabla \boldsymbol{u}_s}} \\ &\quad + \left(\hat{\boldsymbol{\xi}}_d(\dots)_s - \hat{\rho}^s \frac{\partial \hat{\psi}^s(\dots)_s}{\partial \nabla d} \right) \cdot \dot{\overline{\nabla d}} - \left(\hat{\pi}_d(\dots)_s + \hat{\rho}^s \frac{\partial \hat{\psi}^s(\dots)_s}{\partial d} \right) \dot{d} \\ &\quad - \hat{\rho}^s \frac{\partial \hat{\psi}^s}{\partial \dot{d}} \ddot{d} + \left(\phi \hat{\boldsymbol{\tau}}(\dots)_f + \nabla S \otimes \hat{\boldsymbol{\xi}}_S(\dots)_f \right) : \boldsymbol{D} + \mathcal{A} \left(\nabla S \otimes \hat{\boldsymbol{\xi}}_S(\dots)_f \right) : \boldsymbol{A} \\ &\quad + \left(\hat{p}(\dots)_f \nabla \phi - \boldsymbol{f}^{sf} \right) \cdot \boldsymbol{v}_{f/s} - \hat{\rho}^f \frac{\partial \hat{\psi}^f}{\partial \boldsymbol{v}_{f/s}} \overset{\circ}{\boldsymbol{v}}_{f/s} - \hat{\rho}^f \frac{\partial \hat{\psi}^f}{\partial \boldsymbol{D}} \overset{\circ}{\boldsymbol{D}} \\ &\quad + \left(\hat{\boldsymbol{\xi}}_S(\dots)_f - \hat{\rho}^f \frac{\partial \hat{\psi}^f(\dots)_f}{\partial \nabla S} \right) \cdot \overset{\circ}{\overline{\nabla S}} + \left(\mu - \hat{\pi}_S(\dots)_f - \hat{\rho}^f \frac{\partial \hat{\psi}^f(\dots)_f}{\partial S} \right) \overset{\circ}{S} \\ &\quad - \hat{\boldsymbol{h}}(\dots)_f \cdot \nabla \mu - \hat{\rho}^f \frac{\partial \hat{\psi}^f}{\partial \mu} \overset{\circ}{\mu} - \hat{\rho}^f \frac{\partial \hat{\psi}^f}{\partial \nabla \mu} \overset{\circ}{\overline{\nabla \mu}} \geq 0, \end{aligned} \tag{25}$$

where the tensor $\nabla \boldsymbol{v}_{f/s}$ has been decomposed into its symmetric $\boldsymbol{D}$ and antisymmetric part $\boldsymbol{A}$. Noting $\mathcal{A}(\boldsymbol{T}) = (\boldsymbol{T} - \boldsymbol{T}^T)/2$ the antisymmetric part of a tensor $\boldsymbol{T}$ and recalling that $\boldsymbol{\tau}$ is symmetric, the term containing $\boldsymbol{A}$ was obtained using the fact that the double contraction of a symmetric tensor and an antisymmetric tensor vanishes.

Now, since $\overset{\cdot}{\overline{\nabla \boldsymbol{u}_s}}$, $\overset{\cdot}{\overline{\nabla d}}$, $\ddot{\mathrm{d}}$, $\boldsymbol{A}$, $\overset{\circ}{\boldsymbol{v}}_{f/s}$, $\overset{\circ}{\boldsymbol{D}}$, $\overset{\circ}{\overline{\nabla S}}$, $\overset{\circ}{S}$, $\overset{\circ}{\mu}$ and $\overset{\circ}{\overline{\nabla \mu}}$ appear linearly in (25), employing the Coleman–Noll procedure (Coleman and Noll, 1963) yields the following constitutive restrictions:

$$
\begin{aligned}
&\frac{\partial \psi^s}{\partial \dot{d}} = 0, \quad \frac{\partial \psi^f}{\partial \boldsymbol{v}_{f/s}} = 0, \quad \frac{\partial \psi^f}{\partial \boldsymbol{D}} = 0, \quad \frac{\partial \psi^f}{\partial \mu} = 0, \quad \frac{\partial \psi^f}{\partial \nabla \mu} = 0,\\
&\mathcal{A}\left(\nabla S \otimes \hat{\boldsymbol{\xi}}_S(\dots)_f\right) = 0,\\
&\hat{\boldsymbol{\sigma}}'(\dots)_s + \nabla S \otimes \hat{\boldsymbol{\xi}}_S(\dots)_f = \frac{\partial \hat{\rho}^s \hat{\psi}^s(\dots)_s}{\partial \nabla \boldsymbol{u}_s},\\
&\hat{\boldsymbol{\xi}}_d(\dots)_s = \frac{\partial \hat{\rho}^s \hat{\psi}^s(\dots)_s}{\partial \nabla d},\\
&\hat{\boldsymbol{\xi}}_S(\dots)_f = \frac{\partial \hat{\rho}^f \hat{\psi}^f(\dots)_f}{\partial \nabla S},\\
&\hat{\pi}_S(\dots)_f = \mu - \frac{\partial \hat{\rho}^f \hat{\psi}^f(\dots)_f}{\partial S},
\end{aligned}
\tag{26}
$$

leaving the following reduced dissipation inequality:

$$
\begin{aligned}
&-\left(\hat{\pi}_d(\dots)_s + \frac{\partial \hat{\rho}^s \hat{\psi}^s(\dots)_s}{\partial d}\right)\dot{d} + \left(\phi \hat{\boldsymbol{\tau}}(\dots)_f + \nabla S \otimes \hat{\boldsymbol{\xi}}_S(\dots)_f\right) : \boldsymbol{D}\\
&\quad + \left(\hat{p}(\dots)_s \nabla \phi - \boldsymbol{f}^{sf}\right) \cdot \boldsymbol{v}_{f/s} - \hat{\boldsymbol{h}}(\dots)_f \cdot \nabla \mu \geq 0.
\end{aligned}
\tag{27}
$$

In (26) and (27), the densities ρ^s and ρ^f have been included inside the partial derivatives since their respective constitutive dependencies are disjoint from $(\dots)_s$ and $(\dots)_f$. From $(26)_2$, one can deduce that $\nabla S \otimes \boldsymbol{\xi}_S = \boldsymbol{\xi}_S \otimes \nabla S$, which implies that $\left(\nabla S \otimes \boldsymbol{\xi}_S\right)\boldsymbol{\xi}_S = \left(\boldsymbol{\xi}_S \otimes \nabla S\right)\boldsymbol{\xi}_S$, i.e. $\left(\nabla S \cdot \boldsymbol{\xi}_S\right)\boldsymbol{\xi}_S = \left(\boldsymbol{\xi}_S \cdot \boldsymbol{\xi}_S\right)\nabla S$. Therefore, the vectors $\boldsymbol{\xi}_S$ and ∇S are collinear. The corresponding collinearity coefficient κ is introduced and chosen constant for simplicity, so that

$$
\boldsymbol{\xi}_S = \kappa \nabla S = \frac{\partial \rho^f \psi^f}{\partial \nabla S}.
\tag{28}
$$

The reasoning behind deducing this collinearity is similar to that invoked by Abels et al. (2012) (see p.12 therein). Furthermore, Gurtin's invariance argument (Gurtin, 1996) implies that the constitutive functions can depend on $\nabla \boldsymbol{u}_s$ only through the strain tensor of the solid $\boldsymbol{\epsilon} = (\nabla \boldsymbol{u}_s + \nabla \boldsymbol{u}_s^T)/2$, so that $\nabla \boldsymbol{u}_s$ can be replaced here above by $\boldsymbol{\epsilon}$. Finally, a sufficient condition to satisfy (27) is to require that each term be non-negative:

$$
\begin{aligned}
&\beta \dot{d} = \nabla \cdot \frac{\partial \rho^s \psi^s}{\partial \nabla d} - \frac{\partial \rho^s \psi^s}{\partial d},\\
&\phi \boldsymbol{\tau} + \kappa \nabla S \otimes \nabla S = C_{St} \boldsymbol{D},\\
&p \nabla \phi - \boldsymbol{f}^{sf} = C_{Da} \boldsymbol{v}_{f/s},\\
&\boldsymbol{h} = -M \nabla \mu,
\end{aligned}
\tag{29}
$$

where $\beta \geq 0$ is the damage viscosity, $C_{St} \geq 0$ is a Stokes coefficient proportional to the binary fluid viscosity coefficient (in keeping with Newtonian fluids' rheological law (Abels et al., 2012; Gurtin et al., 1995)), $C_{Da} \geq 0$ is a Darcy coefficient inversely proportional to the binary fluid mobility, and $M \geq 0$ is the Cahn-Hilliard mobility. These quantities need not be constant, and their dependencies will be specified later.

3.7. Specification of the free energy

Following the previous thermodynamic analysis, the solid free energy is of the form $\hat{\psi}^s(\boldsymbol{\epsilon}, d, \nabla d)$ and is expressed in the following well-established form (see, e.g., Geelen et al. (2019), Hu et al. (2020, 2021)):

$$
\rho^s \hat{\psi}^s(\boldsymbol{\epsilon}, d, \nabla d) = g(d)\psi_e^A(\boldsymbol{\epsilon}) + \psi_e^I(\boldsymbol{\epsilon}) + G_c h(d, \nabla d),
\tag{30}
$$

where $g(d)$ is a stiffness degradation function, with $g(0) = 1$ and $g(1) = 0$, and ψ_e^A and ψ_e^I denote the active (tensile) and inactive (compressive) parts of the elastic energy, respectively. The critical fracture energy is denoted by G_c, and h is the crack density function defined by

$$
h(d, \nabla d) = \frac{1}{c_0 l_d}\left(w(d) + l_d^2 |\nabla d|^2\right),
\tag{31}
$$

where $c_0 > 0$ is a normalization constant, $w(d)$ is the local dissipation function (Marigo et al., 2016), and l_d is the regularization length for the phase field d.

The fluid free energy is of the form $\hat{\psi}^f(S, \nabla S)$ and is expressed following Cogswell and Szulczewski's formulation (Cogswell and Szulczewski, 2017) as:

$$\rho^f \hat{\psi}^f(S, \nabla S) = \frac{12\gamma}{l_S}\left(f(S) + \frac{l_S^2}{16}|\nabla S|^2\right), \tag{32}$$

where γ is the surface tension between the two fluid constituents, l_S is the regularization length for the phase field S, and $f(S) = S^2(1-S)^2$ is chosen as a double-well potential. Thereby, the gradient coefficient κ discovered in the thermodynamic analysis (28) is given by $\kappa = 3\gamma l_S/2$.

3.8. Fracture phase-field model

Different choices of the functions $g(d)$ and $w(d)$ lead to different fracture phase-field models. Here, we adopt a cohesive fracture model (Geelen et al., 2019; Hu et al., 2020, 2021) so as to control both crack nucleation and propagation. The former is controlled by a nucleation energy ψ_c, acting as a damage threshold, and the latter by the critical fracture energy G_c. Note that such a model allows the regularization length l_d to be prescribed independently of the fracture properties, provided it satisfies an upper bound. Following Hu et al. (2021), the functions $g(d)$ and $w(d)$ are taken to be

$$\begin{aligned} g(d) &= \frac{(1-d)^2}{(1-d)^2 + md(1+d)}, \\ w(d) &= d, \end{aligned} \tag{33}$$

where $m = G_c/c_0 l_d \psi_c$ and $c_0 = 4\int_0^1 \sqrt{w(d)}\mathrm{d}d = 8/3$. To ensure the aforementioned advantageous properties of the cohesive model, the condition $m \geq 1$ should be satisfied (Geelen et al., 2019), which yields the following upper bound for the regularization length:

$$l_d \leq \frac{3G_c}{8\psi_c}. \tag{34}$$

The fracture phase-field evolution equation is then obtained from $(29)_1$, (30) and (34):

$$\begin{aligned} \beta\dot{d} &= \frac{G_c}{c_0 l_d}\left(2l_d^2 \bigtriangleup d - w'(d)\right) - g'(d, \psi_c)\psi_e^A, \\ &= \frac{3G_c}{8l_d}\left(2l_d^2 \bigtriangleup d - 1\right) - g'(d, \psi_c)\psi_e^A, \end{aligned} \tag{35}$$

where the dependence of the degradation function g on the nucleation energy ψ_c has been emphasized. The term $\beta\dot{d}$ accounts for the overall rate-dependency of fracture. A source of this rate-dependency is the viscous effect experimentally observed during fracturing (see Fig. 5b), due to the latent cement that slows down the separation of the beads. A second potential source is the frictional contact between the beads and the two plates of the Hele–Shaw cell.

To complete the phase-field for the fracture part of the model, the irreversibility condition $\dot{d} \geq 0$ is enforced. Finally, the spectral decomposition of the elastic energy, as described in the work of Miehe et al. (2010), is invoked:

$$\begin{aligned} \psi_e^A(\epsilon) &= \frac{\lambda_s}{2}\langle\epsilon_v\rangle^2 + \mu_s \sum_{i=1}^{3}\langle\epsilon_i\rangle^2, \\ \psi_e^I(\epsilon) &= -\frac{\lambda_s}{2}\langle-\epsilon_v\rangle^2 - \mu_s \sum_{i=1}^{3}\langle-\epsilon_i\rangle^2, \end{aligned} \tag{36}$$

where $\langle\cdot\rangle$ denotes the Macaulay brackets, ϵ_v the volumetric strain, ϵ_i the principal strains, and λ_s and μ_s denote the first and second Lamé moduli.

3.9. Binary fluid evolution equations

Substituting $(29)_{2,3}$ into the fluid force balance $(10)_2$ yields:

$$C_{Da}\boldsymbol{v}_{f/s} = -\phi\nabla p - \nabla\cdot(\kappa\nabla S \otimes \nabla S) + \nabla.(C_{St}\boldsymbol{D}). \tag{37}$$

Note that if $C_{Da} > 0$ and $C_{St} = 0$, then (37) reduces to a general form of Darcy's law. Conversely, if $C_{Da} = 0$ and $C_{St} > 0$, then (37) reduces to a general form of Stokes' law. To enforce Darcy's law in the porous medium and Stokes' law in the cracks, one can follow the strategy employed by Wilson and Landis (2016) or Ehlers and Luo (2017), and choose C_{Da} and C_{St} as functions of the phase-field damage d to activate these terms when $d = 0$ and $d = 1$, respectively. In light of the experimental conditions examined in this work, the flow in the cracks is assumed to take the simpler form of a Poiseuille flow between the Hele–Shaw cell plates, which are maintained at a constant separation, whereas the flow in the intact porous medium is assumed to take the form of a Darcy flow. Thereupon, $C_{St} = 0$ and $C_{Da} = \phi^2/(\lambda_1 + \lambda_2)$, where λ_α denote the fluid mobilities. Finally, recalling that $\boldsymbol{w} = \phi\boldsymbol{v}_{f/s} = \boldsymbol{w}_1 + \boldsymbol{w}_2$, a sufficient condition to describe the flow of the two constituents within the current thermodynamic framework is

$$\boldsymbol{w}_\alpha = -\lambda_\alpha\left(\nabla p + \phi^{-1}\nabla\cdot(\kappa\nabla S \otimes \nabla S)\right), \tag{38}$$

which is Darcy's law augmented by a capillary (or Korteweg) stress (Gurtin et al., 1995). More specifically, the fluid mobilities are given by

$$\lambda_\alpha = \frac{k(\phi) k_{r\alpha}(S_\alpha)}{\eta_\alpha}, \tag{39}$$

where k denotes the absolute permeability, $k_{r\alpha}$ the relative permeability of phase α, and η_α the dynamic viscosity of phase α. The absolute permeability is expressed as a function of ϕ following Kozeny–Carman's formula (see, e.g., Coussy (2004)), through

$$k(\phi) = \frac{\phi^3}{(1-\phi)^2}\bar{k}, \tag{40}$$

where $\bar{k}$ is the intrinsic permeability. Importantly for the coupling between poromechanics and fracturing, the porosity is expected to reach $\phi = 1$ in the cracks, whereby the permeability k is expected to diverge. This potential issue is circumvented by imposing an upper bound $k_{max} = H^2/12$, where H denotes the height of the Hele–Shaw cell, in line with the aforementioned assumption of Poiseuille flow within the crack. Thereby, the combination of Darcy flow in the intact porous skeleton and Poiseuille flow in the cracks is obtained through imposing $k = \min(k(\phi), k_{max})$.

As for the relative permeabilities, the model of Fourar and Lenormand (1998) (also used in Cueto–Felgueroso and Juanes's model (Cueto-Felgueroso and Juanes, 2014) in a Hele–Shaw cell setting) derived for viscous coupling in fractures is employed in this work:

$$\begin{aligned} k_{r1} &= S_1^3 + \frac{3}{2\mathrm{M}} S_1(1-S_1)(1+S_1), \\ k_{r2} &= \frac{1}{2} S_2^2(3-S_2), \end{aligned} \tag{41}$$

where constituent 1 is chosen to be the non-wetting (invading) phase and constituent 2 is chosen to be the wetting (defending) phase, and $\mathrm{M} = \eta_2/\eta_1$ is the viscosity ratio.

The Cahn–Hilliard mobility M in $(29)_4$ is then specified following Cogswell and Szulczewski's model (Cogswell and Szulczewski, 2017):

$$M = \frac{k}{\bar{\eta}}, \tag{42}$$

where $\bar{\eta} = 2\eta_1\eta_2/(\eta_1+\eta_2)$ is the harmonic average of the viscosities of the two fluid constituents.

3.10. Model summary

To conclude this theoretical section, a summary of the evolution equations in the model that will be discretized is provided below (43). Since the two constituents are directly related through $S_1 + S_2 = 1$ and $\boldsymbol{h}^1 + \boldsymbol{h}^2 = \boldsymbol{0}$, only the evolution of constituent 1 (the invading fluid) is described; recall the notation $S = S_1$. The model therefore consists of the mass balance for the invading fluid, the total mass balance for the binary fluid, the solid mass balance, the total macro-force balance, and the damage evolution (through the damage micro-force balance), which are respectively given by

$$\boxed{\begin{aligned} &\dot{\overline{\phi S}} + \nabla\cdot\boldsymbol{w}_1(p,\phi) + \phi S\dot{\epsilon}_v = \nabla\cdot M(\phi)\nabla\mu(S), \\ &\dot{\phi} + \nabla\cdot\boldsymbol{w}(p,\phi) + \phi\dot{\epsilon}_v = 0, \\ &\phi = \phi_0 + (1-\phi_0)\epsilon_v + \frac{1-\phi_0}{K_s}p, \\ &\nabla\cdot\left(\boldsymbol{\sigma}'(\boldsymbol{\epsilon},S) - bp\boldsymbol{I}\right) = 0, \\ &\beta\dot{d} = \frac{3G_c}{8l_d}\left(2l_d^2 \triangle d - 1\right) - g'(d,\psi_c)\psi_e^A, \quad \dot{d} \geq 0. \end{aligned}} \tag{43}$$

The porosity evolution Eq. $(43)_3$ derives from integrating the solid mass balance $(5)_1$ (also see equation (3.34) in Borja (2006)) and linearizing the resulting exponential function around the reference state $\{\epsilon_v = 0, p/K_s = 0\}$. This system of Eqs. (43) will be solved for μ, p, ϕ, $\boldsymbol{u}_s$, and d, respectively. It is closed with initial and boundary conditions, and the following system of constitutive equations, given by (38), $(26)_6$, $(12)_2$, (32), $(26)_3$, and (30), as:

$$\begin{aligned} \boldsymbol{w}_\alpha &= -\lambda_\alpha\left(\nabla p + \phi^{-1}\nabla\cdot(\kappa\nabla S\otimes\nabla S)\right), \\ \mu &= \frac{12\gamma}{l_S}\left(f'(S) - \frac{l_S^2}{8}\triangle S\right), \\ \boldsymbol{\sigma}' &= g(d)\frac{\partial\psi_e^A}{\partial\boldsymbol{\epsilon}} + \frac{\partial\psi_e^I}{\partial\boldsymbol{\epsilon}} - \kappa\nabla S\otimes\nabla S. \end{aligned} \tag{44}$$

Note that the third terms in the mass balance Eqs. $(43)_1$ and $(43)_2$ are of second order in terms of the deformation, in contrast to the linear strain–displacement relationship employed for the deformation. Through extensive testing, the retention of these higher order terms in the mass balance equations was found to significantly improve the calibration of simulations to experimental observations. In particular, these terms permit the model to better represent the apparent coupling between the evolution of the saturation front and fracture propagation.

3.11. Dimensionless form

The governing equations can be rendered dimensionless with the assistance of a characteristic length l_0, velocity v_0, fluid viscosity $\eta_0 = \eta_2$, permeability k_0, and surface tension $\gamma_0 = \gamma$. It is also useful to define the characteristic pressure $p_0 = v_0\eta_0/l_0$, fluid mobility $\lambda_0 = k_0/\eta_0$, Cahn–Hilliard mobility $M_0 = k_0/\eta_0 = \lambda_0$, and chemical potential $\mu_0 = \gamma_0/l_0$. In the following, dimensionless quantities are noted with an asterisk. The previous system (43) then becomes

$$\begin{aligned}
&\frac{v_0}{l_0}\dot{\overline{\phi S}}^* + \frac{v_0}{l_0}\nabla^*\cdot \boldsymbol{w}_1^* + \frac{v_0}{l_0}\phi S_1\dot{\epsilon}_v^* = \frac{M_0\gamma_0}{l_0^3}\nabla^*\cdot M^*\nabla^*\mu^*,\\
&\frac{v_0}{l_0}\dot{\phi} + \frac{v_0}{l_0}\nabla^*\cdot \boldsymbol{w}^* + \frac{v_0}{l_0}\phi\dot{\epsilon}_v^* = 0,\\
&\phi = \phi_0 + (1-\phi_0)\epsilon_v + \frac{1-\phi_0}{p_0 K_s^*}p_0 p^*,\\
&\frac{p_0}{l_0}\nabla\cdot\left(\boldsymbol{\sigma}'^* - bp^*\boldsymbol{I}\right) = 0,\\
&\frac{v_0\beta}{l_0}\dot{d}^* = \frac{3G_c}{8l_d}\left(2\frac{l_d^2}{l_0^2}\,\triangle^*\, d - 1\right) - g'(d,\psi_c)\psi_e^A, \quad \dot{d}^* \geq 0.
\end{aligned} \tag{45}$$

Similarly, the dimensionless forms of the secondary Eqs. (44) read:

$$\begin{aligned}
&\boldsymbol{w}_\alpha^* = -\lambda_\alpha^*\left(\frac{\lambda_0 p_0}{v_0 l_0}\nabla^* p^* + \frac{\lambda_0\kappa}{v_0 l_0^3}\phi^{-1}\nabla\cdot(\nabla S\otimes\nabla S)\right),\\
&\frac{\gamma_0}{l_0}\mu^* = \frac{12\gamma_0}{l_S}\left(f'(S) - \frac{l_S^2}{8l_0^2}\,\triangle\, S\right),\\
&p_0\boldsymbol{\sigma}'^* = p_0 g(d)\frac{\partial\psi_e^{A*}}{\partial\boldsymbol{\epsilon}} + p_0\frac{\partial\psi_e^{I*}}{\partial\boldsymbol{\epsilon}} - \frac{\kappa}{l_0^2}\nabla^* S\otimes\nabla^* S.
\end{aligned} \tag{46}$$

The final system of equations in dimensionless form is then given by:

$$\begin{aligned}
&\dot{\overline{\phi S}} + \nabla\cdot\boldsymbol{w}_1 + \phi S_1\dot{\epsilon}_v = \mathrm{Pe}^{-1}\nabla\cdot M\nabla\mu,\\
&\dot{\phi} + \nabla\cdot\boldsymbol{w} + \phi\dot{\epsilon}_v = 0,\\
&\phi = \phi_0 + (1-\phi_0)\epsilon_v + \frac{1-\phi_0}{K_s}p,\\
&\nabla\cdot\left(\boldsymbol{\sigma}' - bp\boldsymbol{I}\right) = 0,\\
&\mathrm{B}\dot{d} = 2{\mathrm{L_d}}^2\,\triangle\, d - 1 - g'(d,\psi_c)\mathrm{D_f}, \quad \dot{d}\geq 0,
\end{aligned} \tag{47}$$

along with

$$\begin{aligned}
&\boldsymbol{w}_\alpha = -\lambda_\alpha\mathrm{Da}\left(\nabla p + \frac{3}{4}\mathrm{Ca}^{-1}\mathrm{L_S}\phi^{-1}\nabla\cdot(\nabla S\otimes\nabla S)\right),\\
&\mu = \frac{12}{\mathrm{L_S}}\left(f'(S) - \frac{{\mathrm{L_S}}^2}{8}\,\triangle\, S\right),\\
&\boldsymbol{\sigma}' = g(d)\frac{\partial\psi_e^A}{\partial\boldsymbol{\epsilon}} + \frac{\partial\psi_e^I}{\partial\boldsymbol{\epsilon}} - \mathrm{K}\nabla S\otimes\nabla S,
\end{aligned} \tag{48}$$

where we have dropped the asterisk notation for clarity. The dimensionless groups employed in the above are given by

$$\begin{aligned}
&\mathrm{Pe} = \frac{v_0 l_0^2}{M_0\gamma_0}, && \mathrm{Ca} = \frac{\eta_0 v_0}{\gamma_0}, && \mathrm{Da} = \frac{k_0}{l_0^2},\\
&\mathrm{K} = \frac{\kappa}{p_0 l_0^2}, && \mathrm{M} = \frac{\eta_2}{\eta_1}, && \mathrm{L_S} = \frac{l_S}{l_0},\\
&\mathrm{B} = \frac{8l_d v_0\beta}{3l_0 G_c}, && \mathrm{D_f} = \frac{8l_d\psi_e^A}{3G_c}, && \mathrm{L_d} = \frac{l_d}{l_0},
\end{aligned} \tag{49}$$

denoting the Péclet number, the capillary number, the Darcy number, the Korteweg number, the viscosity ratio (appearing indirectly through (41)), the normalized saturation regularization length, the damage viscosity number, the fracture driving force, and the normalized damage regularization length, respectively. The two first rows represent groups associated with fluid fields, whereas the third row represents the groups associated with solid fields. Note that there are only five independent fluid groups since $\mathrm{Pe} = 4\mathrm{Da}^{-1}\mathrm{Ca}/3$. The expression for the Péclet number matches the one obtained by Abels et al. (2012) for instance. Recall that $\kappa = 3\gamma l_S/4$.

In practice, it is also useful to define a modified capillary number Ca^* introduced by Holtzman et al. (2012) and employed in the experiments (Meng et al., 2023) considered in this work. This number is the ratio of the driving force (i.e., the viscous pressure drop δp_{vis}) to the capillary pressure force δp_{cap}. The former can be estimated as

$$\delta p_{vis} \sim \frac{\eta_o w_i l_0}{k_0} \sim \frac{\eta_o q l_0}{H\delta k_0}, \tag{50}$$

where w_i is the injection Darcy flux of water, q is the corresponding volumetric flow rate, which scales as $q \sim w_i h\delta$, H is the height of the Hele–Shaw cell, δ is a characteristic grain size, which will be the diameter of the beads used in the experiments studied in this work, and the characteristic length l_0 is taken as the radius r_o of the Hele–Shaw cell. The capillary pressure drop is estimated as

$$\delta p_{cap} \sim \frac{\gamma}{\delta}. \tag{51}$$

Thereby, the modified capillary number reads

$$\mathrm{Ca}^* \sim \frac{\delta p_{vis}}{\delta p_{cap}} \sim \frac{q\eta_o l_0}{\gamma h k_0} \sim \mathrm{Ca}\frac{l_0\delta}{k_0}. \tag{52}$$

Given the assumption of viscous-dominated flow, $\mathrm{Ca}^{-1} \ll 1$, and therefore $\mathrm{Pe}^{-1} \ll 1$, but also $\mathrm{K} \ll 1$, so that one can anticipate that the terms containing these numbers should not play a significant role. That said, the Cahn–Hilliard term on the right side of (47) plays an important interface regularization role, as mentioned by Cogswell and Szulczewski (2017).

4. Numerical study

In this section, the ability of the model to reproduce the salient aspects of recent experimental observations, and in particular, to recover a phase diagram distinguishing two flow regimes is examined. Simulations are then employed to make predictions for system responses corresponding to regions of parameter space that are beyond recent experimental observations.

4.1. Numerical implementation

The system of Eqs. (43), (44) is discretized through the finite-element method and implemented within the Multiphysics Object Oriented Simulation Environment (MOOSE) (Permann et al., 2020). For the coupling with phase-field fracture, the RACCOON extension https://github.com/hugary1995/raccoon is used. The resulting system of equations is solved in a staggered fashion, whereby the poromechanical Eqs. $(43)_{1-4}$ and the damage Eq. $(43)_5$ are solved iteratively at each time step until convergence is reached. For the damage equation, the irreversibility constraint $\dot{d} \geq 0$ is enforced with a primal–dual active set strategy (Hu et al., 2020). Each of the two sub-systems of nonlinear equations are solved with the Newton–Raphson method. Therein, the rate terms are integrated in time using an implicit backward Euler approximation. Finally, the matrix inversions are obtained through an LU decomposition, using the preconditioner MUMPS (Multifrontal Massively Parallel sparse direct Solver) https://mooseframework.inl.gov/modules/porous_flow/solvers.html available within the PETSc library.

4.2. Boundary-value problem and initial conditions

Consider the two-dimensional annular domain defined by an inner and outer radius, as shown in Fig. 2. The boundary conditions are prescribed on the inner and outer surfaces in a manner meant to approximate the aforementioned experimental setup. The values of all model parameters contained within the boundary conditions are provided in Table B.1.

For the mechanical fields, boundary conditions that approximate fluid injection at a constant flow rate at the inner boundary and constrained outflow conditions at the outer boundary are prescribed. In particular, at the inner boundary, the Darcy flux of the invading fluid is fixed at a value w_i chosen to match the experimental injection pressure curve. The pressure is then calculated at each time step by taking the average of its values at every node of the inner boundary https://mooseframework.inl.gov/modules/porous_flow/thm_example.html, denoted by $\tilde{p}_i$, and applied to the total stress as a boundary condition at the subsequent step (Rehbinder, 1995).

At the outer boundary, the pressure is fixed to 0 (the air pressure in the laboratory, used as a reference pressure) and the displacement field is held fixed, consistently with the mechanical constraint on the cemented bead network in this region. Finally, zero Neumann boundary conditions on the damage field are imposed at both boundaries, as is standard in phase-field models of fracture.

For the saturation field S, Dirichlet conditions of $S = 1$ and $S = 0$ are prescribed at the inner and outer boundaries, respectively. These conditions reflect the fact that the invading fluid enters at the inner boundary, while the defending fluid exits the domain at the outer boundary. The latter boundary condition obviously limits the applicability of the model to the point in time when the leading edge of the invading fluid just reaches the outer boundary.

The boundary conditions on the chemical potential are inspired by the work of Dong (2014). At the inner boundary, the chemical potential is fixed to a small value $\mu_i > 0$ to facilitate the incoming flow of fluid. On the outer boundary, Dong's zero-flux condition is replaced by a Dirichlet boundary condition $\mu_o > 0$, since a zero-flux condition on the chemical potential was found to lead to spurious nucleation of the invading fluid phase. In the calibration of the simulations against the experimental observations, the point in time when the injection pressure peaks is observed to be sensitive to μ_o. Accordingly, the magnitude of μ_o is adjusted to obtain the best match between the simulated and experimental injection curves.

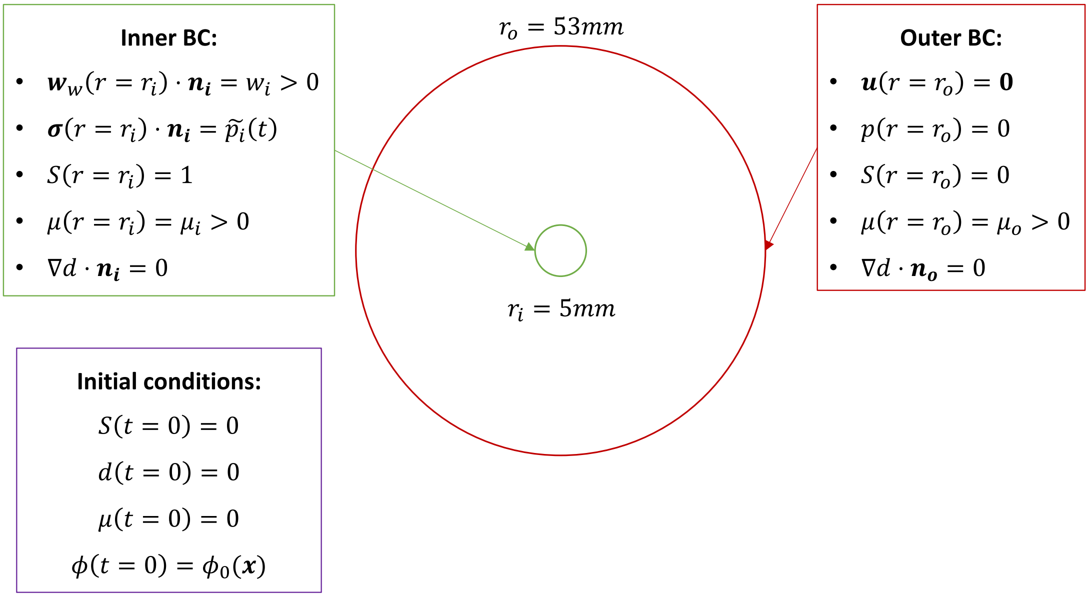

Fig. 2. Schematic of the boundary-value problem along with boundary and initial conditions. For the boundary conditions, $\boldsymbol{n}_i$ and $\boldsymbol{n}_o$ denote the inward normal and outward normal at the inner and outer boundaries, respectively.

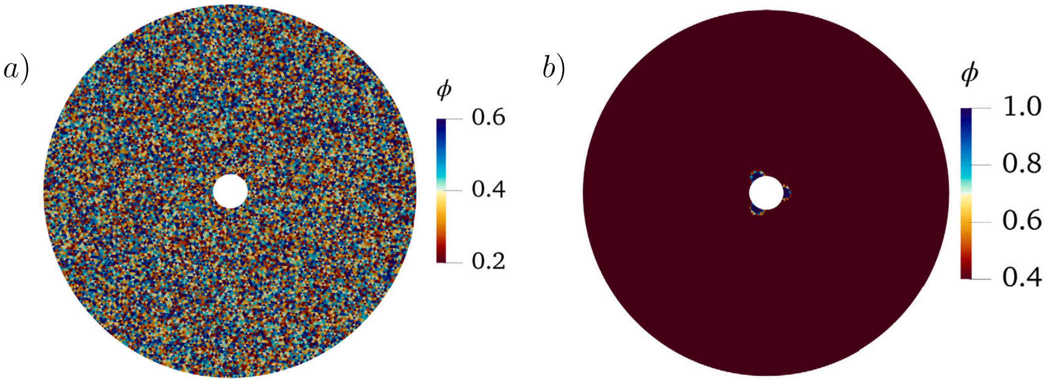

Fig. 3. Initial porosity fields used in this work. (a) Random porosity field with mean value $\bar{\phi} = 0.4$. (b) Constant porosity field with existing porosity pockets near the inner boundary employed in the mesh convergence study.

The initial conditions, as indicated in Fig. 2, consist in setting all variables to 0, except the porosity field. In this work, the influence of the microstructure stemming from the arrangement of the beads is not examined in detail. Instead, a continuum perspective and focus on the influence of the hydro-mechanical parameters is adopted. However, some heterogeneity in the initial conditions is required to break the inherent symmetry of the problem and facilitate localization. To effect this, the initial porosity field is assumed to be uniformly random. More precisely, a porosity value, varying between 0.2 and 0.6, is randomly assigned to each mesh element (see Fig. 3a). This ensures that the mean porosity value is 0.4, which corresponds to the measured experimental value. This particular range is motivated by what results from the use of a moving window approach to upscale the porosity, as described in Peco et al. (2019). In that approach, a continuum approximation to the initial porosity is obtained by explicitly calculating the volume fraction of beads within a small, circular window centered at each point in the domain. Such a wide range was also found to be necessary to sufficiently break the symmetry of the response in the resulting simulations.

In addition, to establish spatial convergence with the discretization, a different porosity field that does not vary with mesh refinement is considered. To construct such a field, a constant porosity field is used with three small circular regions of high porosity near the inner boundary, giving rise to the initial porosity field shown in Fig. 3b.

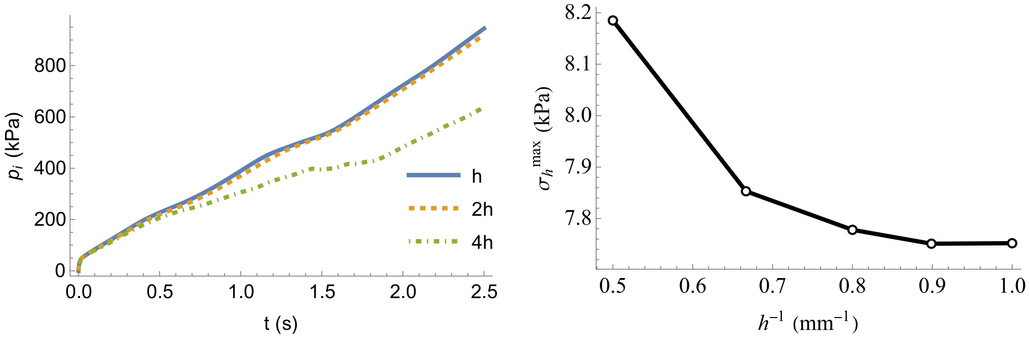

Fig. 4. Graphs of the injection pressure over time and of the maximum hoop stress for different mesh refinements, with reference element size $h = 1.0\,\mathrm{mm}$.

4.3. *Spatial convergence study*

The ability of the model and accompanying discretization to obtain spatial convergence in selected quantities of interest is first established. A series of simulations with increasing mesh refinement for the initial boundary-value problem described in Fig. 2 using the initial porosity field shown in Fig. 3b are performed. Fig. 4 shows plots of the evolution of the injection pressure over time and of the maximum hoop stress for a reference mesh with uniform spacing $h = 1.0\,\mathrm{mm}$ (20,672 elements) and coarser meshes. The results indicate that the reference mesh satisfies the requirement of mesh convergence. Accordingly, subsequent studies reported in this manuscript use unstructured meshes of linear triangular elements with mesh spacing $h = 1\,\mathrm{mm}$. This level of spatial resolution is sufficient to capture the regularization lengths indicated in Table B.1. More precisely, the phase field interfaces for S and d span approximately four elements.

4.4. *Reproduction of a given experiment*

The extent to which the model can reproduce qualitative aspects of a given Hele–Shaw experiment is now examined. In particular, consider an experiment in which the cement fraction is 1.2%, the oil viscosity is $0.29\,\mathrm{kPa\,s}$, and the injection flow rate is $100\,\mathrm{mL/min}$. In line with the provided experimental parameters, the simulation parameters for this problem are summarized in Table B.1 in Appendix. The random field shown in Fig. 3a is used as an initial condition for the porosity.

The Hele–Shaw cell is represented in the simulations by an annulus of inner radius $r_i = 5\,\mathrm{mm}$ and outer radius $r_o = 53\,\mathrm{mm}$, as indicated in Fig. 2. The inner radius is estimated by measuring the average initial radius of the inner cavity delimited by the beads in the experiment. Within the experimental estimated range of values for the initial average permeability, a value toward the lower end of this range is found to work best in the simulations, namely $0.0015\,\mathrm{mm}^2$. More precisely, this value for the average permeability was found to yield the best match with the experiments for the velocity of the invasion front in the intact porous medium. The elastic moduli of the porous skeleton are estimated from experimental measurements (Meng et al., 2022b).

The simulation results are obtained with fracture parameters that scales with the cement volume ratio C as follows. For the fracture toughness, the experimentally-determined relationship (1) is adopted. The nucleation energy ψ_c governs damage initiation. Assuming that crack nucleation occurs at a critical value p_c of the injection pressure, a simple estimate of the critical fracture energy is given by (see equation 24 in Geelen et al. (2019))

$$\psi_c = \frac{p_c(C)^2}{2E}. \tag{53}$$

From the experimental measurements, the critical injection pressure p_c that corresponded to crack initiation appears to scale linearly with the cement volume ratio, such that $p_c = \alpha C$. A magnitude of $\alpha = 1\,\mathrm{kPa}$ is found to provide a good match with the experimental observations for crack initiation as a function of cement volume ratio. Finally, the damage viscosity β in $(43)_5$ is also set to be an increasing function of the cement ratio. The precise relationship is given in the next section, when the simulation results are calibrated against experimental observations.

Fig. 5 provides snapshots of the experimental results at the start of the experiment and at $t = 2.0\,\mathrm{s}$, along with simulation results of the damage and porosity fields at the corresponding times. All simulation results are shown in the reference configuration. The time $t = 2.0\,\mathrm{s}$ corresponds to the moment in the experiment when the injection pressure reaches a plateau of approximately $470\,\mathrm{kPa}$ (see Fig. 7). To facilitate comparisons between the experimental and simulation results at $t = 2.0\,\mathrm{s}$, the water front is indicated with white contour lines. For the experiment, this contour was extracted manually based on the color of the fluid (blue for water vs. gray for oil). The fractured surfaces are also sketched on the experimental image as blue contours. In the simulation results, the white contour corresponds to the saturation level $S = 0.5$. For reference, the full saturation field at the start of the simulation and at $t = 2.0\,\mathrm{s}$ is shown in Fig. 6.

An inspection of the results in Fig. 5 indicates that the model is able to replicate the main salient features of the water invasion. First, there are three main cracks, corresponding to regions of porosity equal to 1 in the simulations, preceded by partially damaged

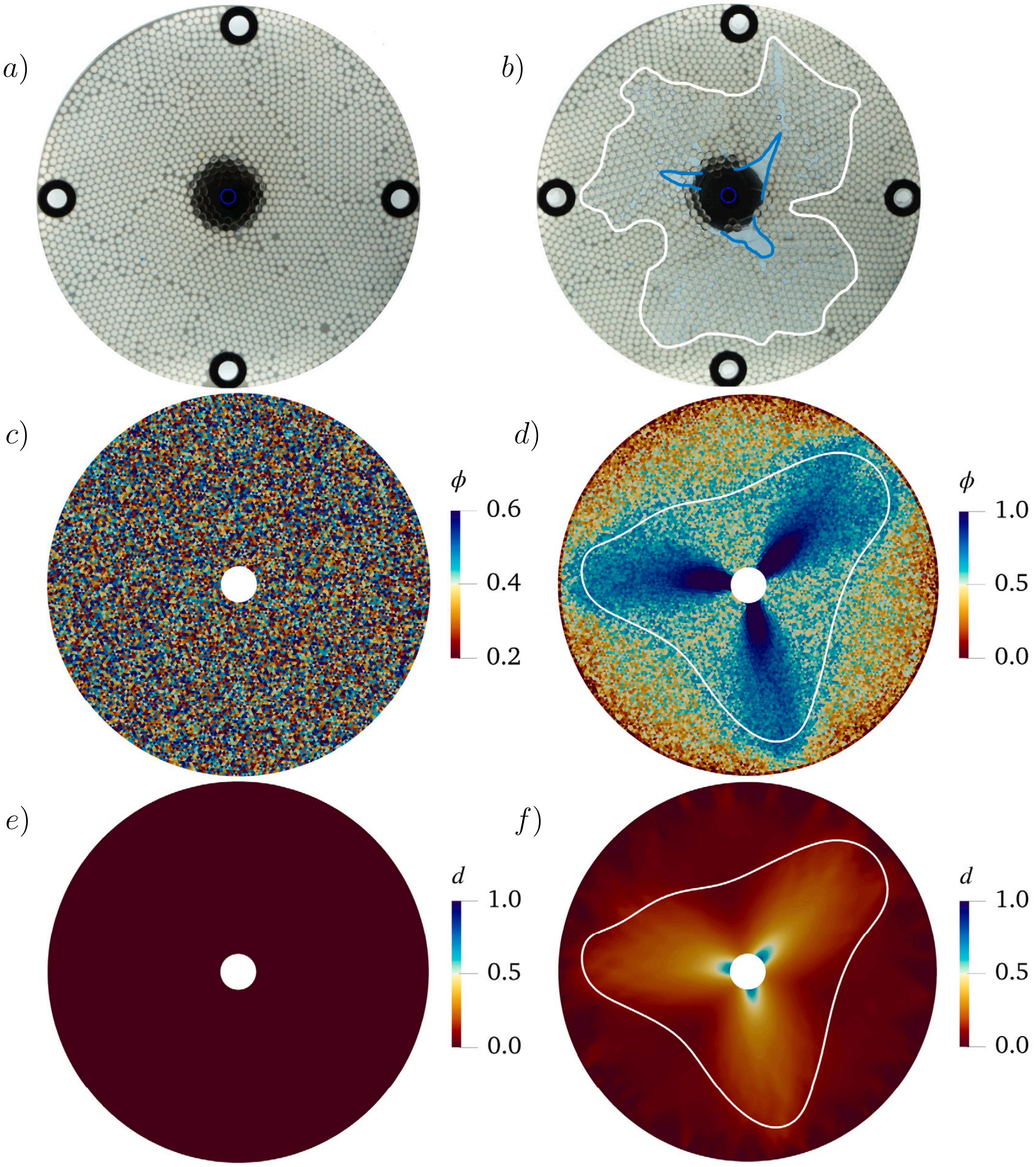

Fig. 5. Comparison of the experimental results (a,b) with the simulation results (c, d, e, f). The left and right columns correspond to $t = 0$ and $t = 2.0\,\mathrm{s}$, respectively. The second row shows the porosity field, while the third row shows the damage field. In the images on the right, the white contours indicate the leading edge of the invading fluid front and the blue contour in (b) indicates the border of fully fractured zones.

zones. At $t = 2.0\,\mathrm{s}$, in the reference configuration, the cracks obtained in the simulations measure around $11\,\mathrm{mm}$ on average, similar to the experiment. Secondly, at $t = 2.0\,\mathrm{s}$, the saturation front from the simulation lies ahead of the cracks at a distance of $45\,\mathrm{mm}$ from the center, calculated from an average of the distance of the three main invasion branches. The analogous distance in the experiment is found to be approximately $44\,\mathrm{mm}$. Both the experimental and simulation results indicate three types of fluid invasion: (1) into fully intact regions; (2) into partially open regions; and (3) into fully open regions (where the porosity $\phi = 1.0$). Note that a fully open region (where $\phi = 1$) does not necessarily coincide with a fully damaged region (where $d = 1$). This is due to the damage viscosity term $\beta\dot{d}$. In other words, fully open regions can still bear some tensile loading. This is justified by the presence of residual strands of glue observed in the experiment (see Fig. 5b), which are assumed sufficiently small so as not to impede flow but large enough to still allow the skeleton to transmit tractions. As a result, particularly in the present setting with viscous damage, it is important to interpret hydraulic cracks through the assessment of the porosity field and not the damage field.

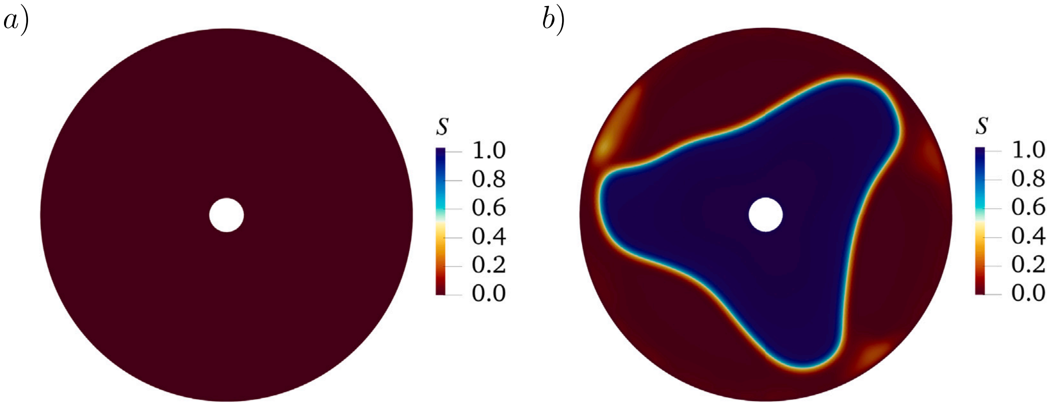

Fig. 6. Saturation field corresponding to the white contour shown in Fig. 5 at $t = 0$ (a) and $t = 2.0\,\mathrm{s}$ (b).

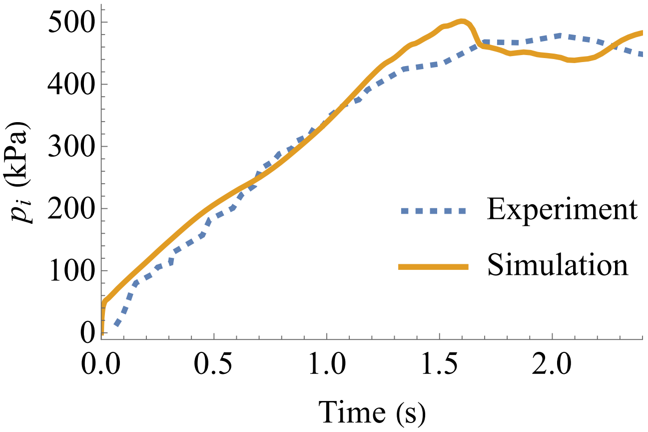

Fig. 7. Injection pressure curve obtained from the experiment and matched in the simulation.

Fig. 7(a) provides a comparison of the injection pressure as measured in the experiment to that extracted from the simulation. Note that the imposed Darcy flux w_i was adjusted to obtain a good match with the initial portion of the pressure signal, in particular over the time period $t \in [0, 1.0]$s. A constant value of $w_i = 50\,\mathrm{mm/s}$ was found to provide the best match. Interestingly, the experimental and simulation results compare favorably even after that initial period, with both exhibiting a plateau starting around $t = 1.7\,\mathrm{s}$. In both the experiment and the simulation, the injection pressure peaks at approximately $470\,\mathrm{kPa}$. The decrease of the rate of injection pressure coincides with the decrease of the rate of the average damage in the domain, as shown in Fig. C.14 in Appendix C. The delay between the damage plateau and the injection pressure plateau may be attributable to the damage viscosity. Fig. 8 compares the volumetric strain response between the simulation and the experiment at $t = 2.0\,\mathrm{s}$. In both cases, three regions of tensile volumetric strain are observed to develop out of the injection site. For both the simulation and the experimental results, these regions correspond to zones in which fracturing has occurred. On one hand, the high tensile regions in the experiment are somewhat larger and more diffuse than those in the simulation. On the other, the transition from regions of tensile volumetric strain to compressive volumetric strain is more abrupt in the experiment, at least in the areas between the three main branches. Finally, the outermost boundary is seen to be in a state of compressive volumetric strain with a spatial variation that is more uniform in the experiment than the simulation. This discrepancy may be due to the fact that the four outer clamps in the experiment are not explicitly modeled in the simulation. Alternatively, it could also be due to the fact that in the experiments the outer boundary containing the beads within the domain is not strictly rigid, and therefore allows some release of elastic energy.

Finally, Fig. 9 shows the simulation results for the pressure, hoop stress, permeability, and Darcy flux of water at $t = 2.0\,\mathrm{s}$. To facilitate the interpretation of the results, a white contour line is once again used to denote the $S = 0.5$ saturation front. The peak values of the pressure field can be seen to be concentrated within the invading fluid phase, as expected. The hoop stress is observed to be somewhat similar to the volumetric strain. The permeability is largest within the highly-damaged regions, until it reaches an upper bound of $(1.92^2/12 = 0.31\,\mathrm{mm}^2)$. Recall that this upper bound follows from assuming a Poiseuille flow confined by the two plates of the Hele–Shaw cell. As anticipated, the Darcy flux is maximal in the damaged areas and at the water front.

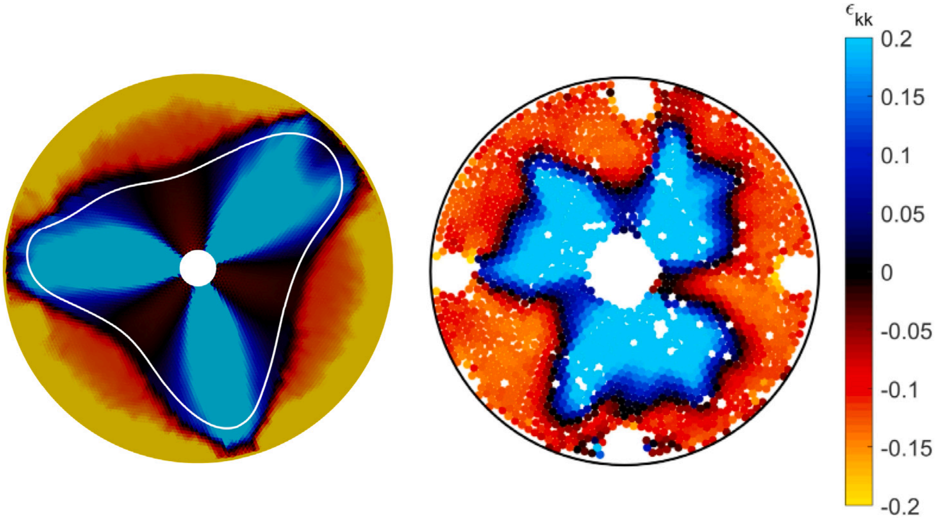

Fig. 8. Comparison of the volumetric strain field between the simulation (left) and the experiment (right). A fluid saturation of $S = 0.5$ is indicated in the simulation result as a white contour.

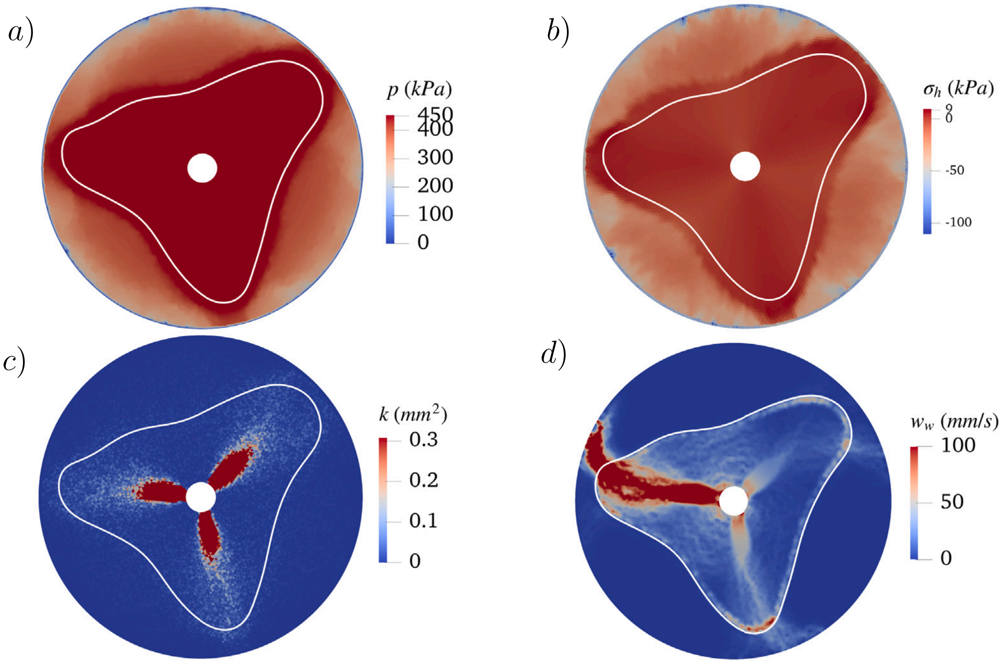

Fig. 9. Simulation results for: (a) the pressure; (b) the hoop stress; (c) the permeability; and (d) the magnitude of the Darcy flux of water.

4.5. Reproduction of an experimental phase diagram

Experiments were conducted using monolayers of cemented beads with varying degrees of cement and a range of injection rates (Meng et al., 2023). As expected, larger cement volume fractions gave rise to layers with increased fracture resistance. Fig. 10 shows a phase diagram delineating two regimes of response as a function of the modified capillary number Ca^* and the cement volume ratio C. The symbols in the diagram correspond to individual experiments or simulations, with the symbol type and color indicating the source and the observed flow regime, respectively.

The simulation results appear to replicate the phase diagram reasonably well, as indicated in Fig. 10. The phase diagram can be interpreted as follows. For a given cement ratio, fluid injection at relatively low capillary numbers gives rise to porous invasion without any fracturing of the monolayer. As the capillary number is increased, the mechanical loading on the monolayer becomes

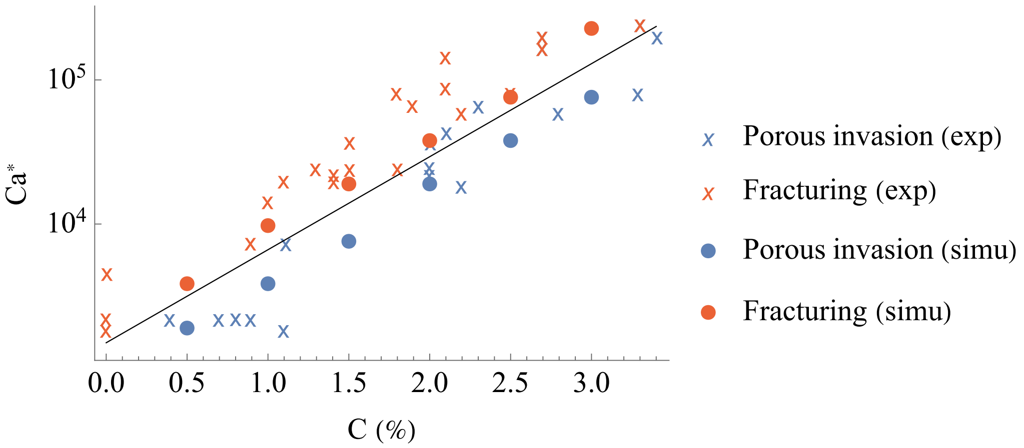

Fig. 10. Phase diagram representing the modified capillary number Ca* vs. the cement volume ratio C. An exponential separatrix (black line) was found to separate a porous invasion regime from a fracturing regime for both the experimental and numerical results.

large enough to give rise to fracturing. Note that the transition from porous invasion to fracturing regime is progressive, in the sense that a simulation result labeled as porous invasion may display some small cracks, albeit with little influence on the invasion pattern. Throughout this work, these two regimes are differentiated by measuring the length of the longest crack. If this length is larger (resp. smaller) than an arbitrarily small length, then the simulation result is labeled as belonging to the fracturing regime (resp. porous invasion regime). Following the discussion in Section 4.4 regarding the importance of interpreting hydraulic cracks through the porosity field, crack lengths are calculated based on the distance from the center of the domain to the end of regions with porosity $\phi = 1$. The outcome of both experiments and simulations is that the threshold separating porous invasion from fracturing was found to scale exponentially with the cement volume ratio, as indicated by the solid black line in Fig. 10.

It bears emphasis that a key parameter in the model was adjusted to yield the best match between the experimental and simulation results in this phase diagram. As mentioned in Section 4.4, the damage viscosity β is assumed to be an increasing function of the cement volume ratio C. A relatively simple relationship that appears to provide a good match with the experimental phase diagram is $\beta = c\sqrt{C}$, with $c = 65.7\,\mathrm{kPa\,s}$ as the damage viscosity coefficient. The physical basis for this particular value for c has yet to be established, but in principle it could be connected to various sources of rate dependency, such as the viscoelasticity of the cementing glue. Having sufficiently calibrated the model, in the remainder of this paper, simulations are employed to explore regions of the parameter space well outside the reach of the experimental setup.

4.6. Effect of the fracture parameters ψ_c, G_c, and β

Before examining the influence of the main hydraulic parameters (permeability and viscosity), results illustrating the sensitivity of the model to the fracture parameters are reported. The fracturing response of the system is governed by 3 parameters in the model: the nucleation energy ψ_c (crack initiation), the fracture toughness G_c (crack propagation), and the damage viscosity β (rate effects). The sensitivity of the simulation results to variations in each of these parameters is illustrated in Fig. 11. The middle column in the Figure corresponds to the base state that was used to make the comparisons in Section 4.4. For the sake of comparison, all simulation results are shown when the saturation front is at a similar distance from the outer boundary.

As expected, increasing either the fracture toughness G_c or the damage viscosity β is observed to inhibit crack propagation. Less expected is the effect of the nucleation energy ψ_c: while increasing its value delays crack initiation, the final cracks are observed to progress further in the domain. This may be explained by the accumulation of strain energy in the system while crack initiation is prevented until the energy reaches the higher threshold.

4.7. Phase diagram representing fracturing number vs. branching number

A wide range of the parameter space is now explored to infer the types of possible flow regimes predicted by the model. As described in the introduction, the model is expected to indicate various types of viscous flows, namely porous invasion, invasive and non-invasive fracturing, in possible combination with viscous fingering. The primary model parameters determining the type of flow are found to be, unsurprisingly, the 3 main fluid parameters η_o, η_w, and k_0, which are therefore widely varied in this section. Note that the characteristic permeability k_0 is taken as the initial average permeability in this section.

First, to determine whether the flow is of fracturing type or not, the fracturing number, denoted by N_f, is employed. Taking inspiration from Holtzman et al. (2012), the fracturing number is defined as the ratio of the driving force to the resisting force. The

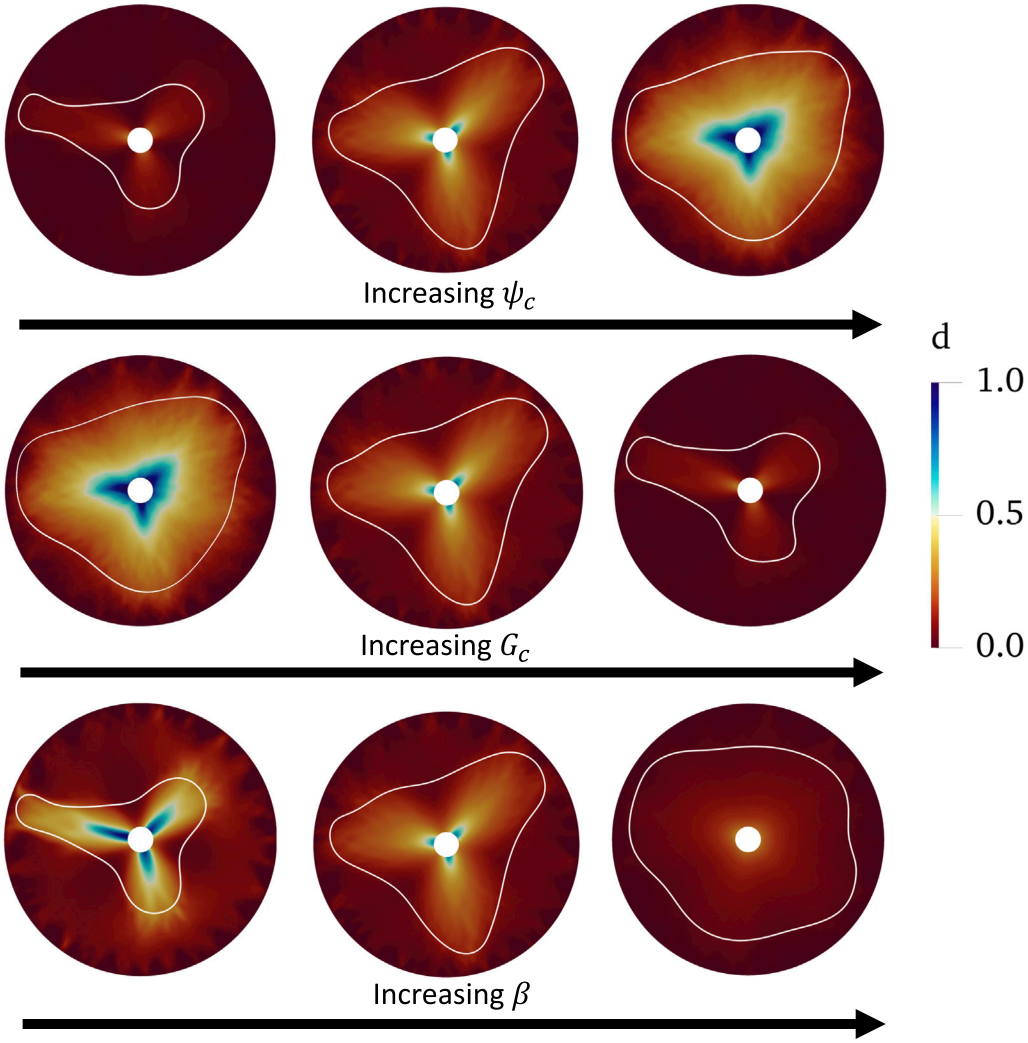

Fig. 11. Effect of the fracture parameters ψ_c (nucleation energy), G_c (fracture toughness), β (damage viscosity). The damage field is shown along with the white contour of the saturation front. The middle column corresponds to a reference simulation common to the three rows, obtained with the fracture parameters values stemming from the experimental study. The left and right columns are obtained by dividing and multiplying these reference values by 10, respectively. The simulations results are shown when the saturation front is at a same certain distance from the outer boundary.

driving force is taken to be the viscous pressure drop δp_{vis} introduced in (50). The resisting force is the critical injection pressure δp_{cri} at which the flow regime transitions from porous invasion to fracturing. The fracture number thus reads:

$$\mathrm{N}_f = \frac{\delta p_{vis}}{\delta p_{cri}}. \tag{54}$$

While the driving force characterizes the invasion and contains only flow parameters, the resisting force characterizes the fracture resistance of the medium and depends on pertinent strength quantities such as the cement fraction. In this section, the fracture parameters are held fixed and, therefore, the value of δp_{cri} is common for all simulations.

Second, to further characterize the type of flow within the fracturing and porous invasion regimes, a new dimensionless number is constructed, called the branching number and denoted by N_b, given by

$$\mathrm{N}_b = \frac{\eta_w l_0^2}{\eta_o k_0}. \tag{55}$$

Note that the branching number is related to the Darcy number and the mobility ratio defined in (49) through $\mathrm{N}_b = \mathrm{M}^{-1}\mathrm{Da}^{-1}$. For a fixed fracturing number N_f, varying the branching number N_b was found to give rise to two types of flow. In the porous invasion

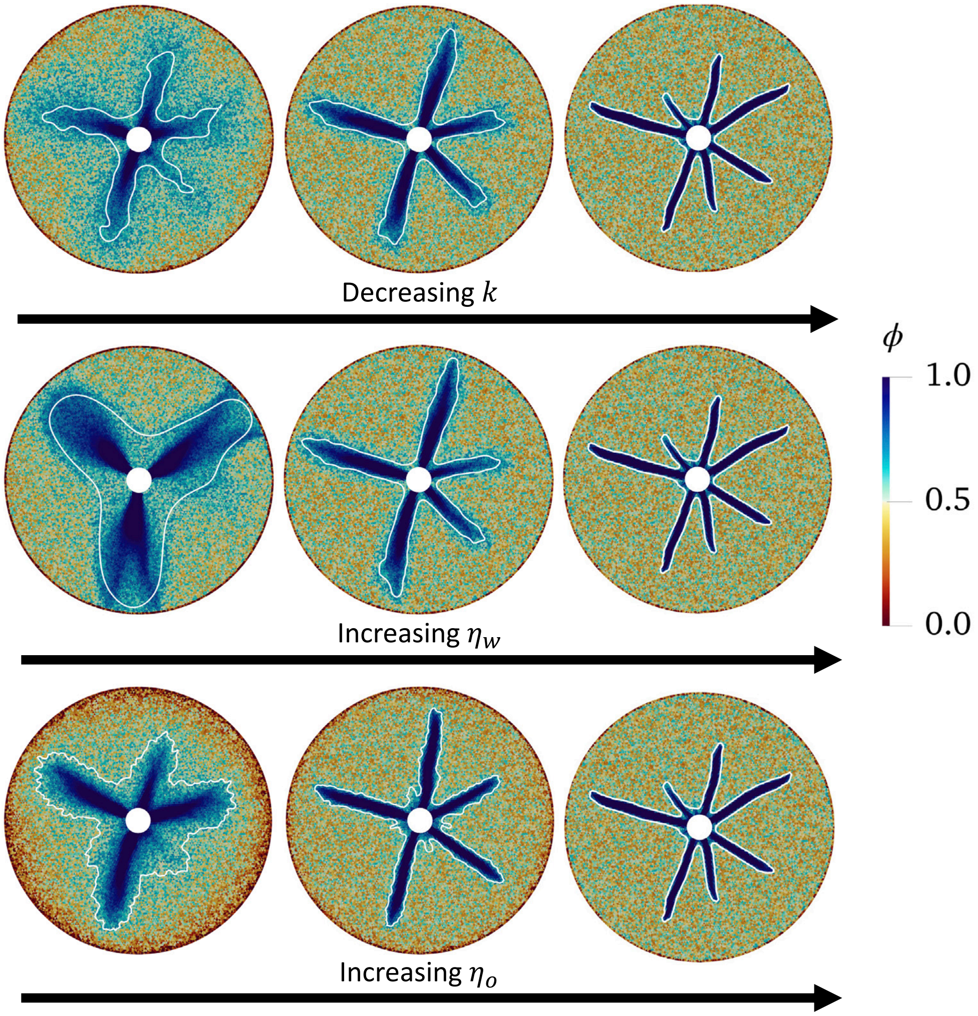

Fig. 12. Plots of the porosity field and saturation front (white contour) illustrating the sensitivity to changes in various flow parameters. Influence on the branching pattern of permeability (from left to right: $\bar{k} = 5 \times 10^{-2}\,\mathrm{mm}^2$, $\bar{k} = 10^{-2}\,\mathrm{mm}^2$, $\bar{k} = 10^{-3}\,\mathrm{mm}^2$, at fixed $\eta_o = 1\,\mathrm{kPa\,s}$ and $\eta_w = 10^{-3}\,\mathrm{kPa\,s}$), of invading fluid viscosity η_w (from left to right: $\eta_w = 10^{-6}\,\mathrm{kPa\,s}$, $\eta_w = 10^{-4}\,\mathrm{kPa\,s}$, $\eta_w = 10^{-3}\,\mathrm{kPa\,s}$, at fixed $\eta_o = 1\,\mathrm{kPa\,s}$ and $\bar{k} = 10^{-3}\,\mathrm{mm}^2$), and of defending fluid viscosity (from left to right: $\eta_o = 10^{-3}\,\mathrm{kPa\,s}$, $\eta_o = 10^{-2}\,\mathrm{kPa\,s}$, $\eta_o = 1\,\mathrm{kPa\,s}$, at fixed $\eta_w = 10^{-3}\,\mathrm{kPa\,s}$ and $\bar{k} = 10^{-3}\,\mathrm{mm}^2$).

regime ($\mathrm{N}_f < 1$), low values of N_b indicate a uniform porous invasion, whereas large values of N_b indicate a viscous fingering instability. The number of branches of this instability was found to increase with N_b. In the fracturing regime ($\mathrm{N}_f > 1$), low values of N_b indicate invasive fracturing, whereas large values of N_b indicate non-invasive fracturing. The number of “crack branches” was found to increase with N_b.

To illustrate these observations, Fig. 12 shows the individual influence of the main parameters of N_b on the type of flow. A first intuitive result is that decreasing the permeability tends to result in the invading fluid flow being more confined to the cracks, thereby indicating a transition from invasive to non-invasive fracturing. Non-invasive fracturing is characterized by the invading fluid front being confined to the open channels that form. As for the influence of the fluid viscosities, similar trends are observed with increasing η_w and η_o, as shown in the figure. Note that while k_0 and η_w play a role that is consistent with the aforementioned rationale behind the branching number, it is not the case for η_o, at least individually. However, as a group, the branching number does play the role explained above, for fixed values of the fracturing number. Finally, the left simulation result of the third row of Fig. 12 displays a new type of flow, which is the combination of the fracturing regime and viscous fingering. However, the branching number alone is not sufficient to identify the parameter space where this regime dominates; this will be done in combination with the fracturing number later in this section.

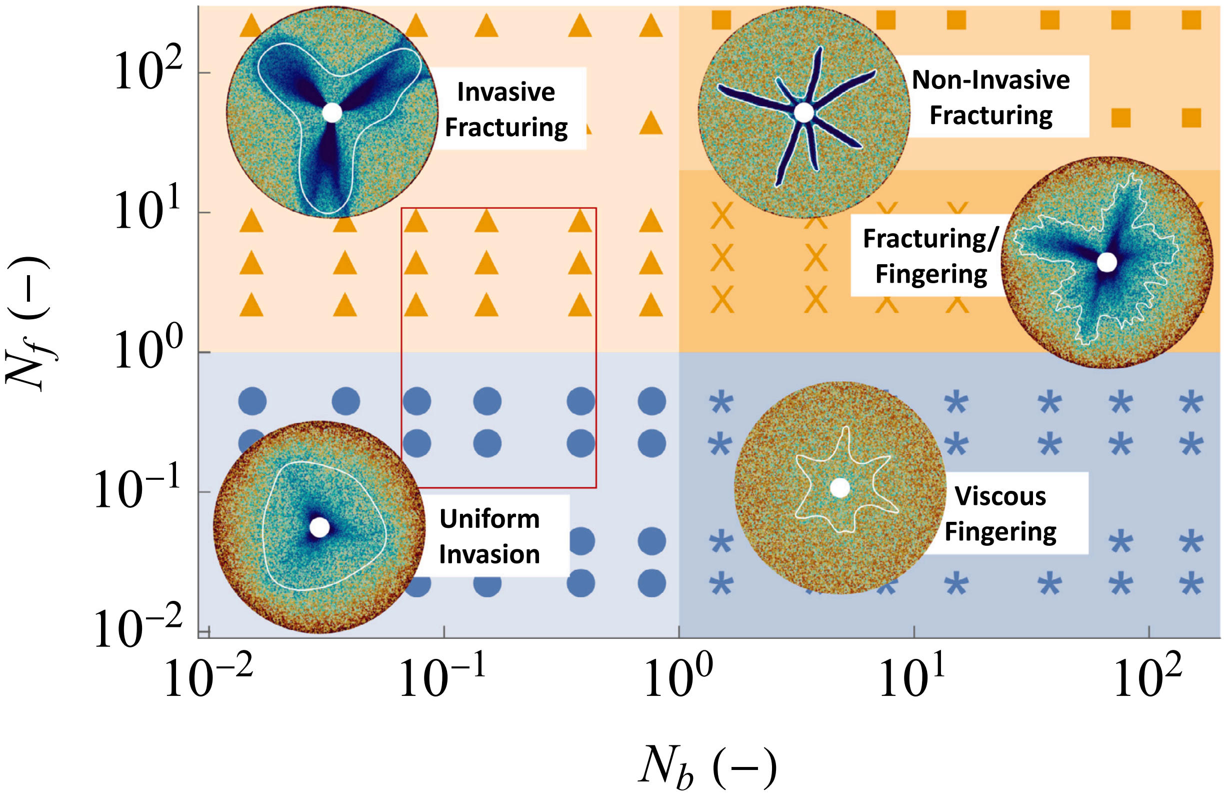

Fig. 13. Phase diagram of the fracturing number N_f vs the branching number N_b, mapping the five types of flow regimes. The red rectangle indicates the region of diagram explored by the experiments. The circular inserts are simulation results representing the porosity field along with the saturation front in white.

During extensive testing, the simulations indicated that although the invading fluid viscosity η_w has an effect on the branching pattern, it has a very limited influence on the fracture onset. This is consistent with experimental observations by Zhou et al. (2010) as well as the results described in Carrillo and Bourg (2021).

To build a phase diagram of the fracturing number N_f vs. the branching number N_b representing all possible flow regimes, a large number of simulations are conducted over wide ranges of the parameters η_o, η_w, k_0. The resulting phase diagram is shown in Fig. 13, with each symbol corresponding to an individual simulation and positioned at the corresponding values of N_b and N_f. For the resulting values of N_b, the characteristic length was chosen as the inner radius of the Hele–Shaw cell (i.e., $l_0 = r_i = 5\,\text{mm}$).

The particular flow regime indicated by each simulation is tagged as either a blue circle (uniform invasion), a blue star (viscous fingering), an orange triangle (invasive fracturing), an orange square (non-invasive fracturing), or an orange cross (fracturing/fingering). The resulting regions where each type of flow dominates are also colored to help indicate threshold values for N_f or N_b that separate various regimes.

Note that N_b and N_f are inherently different since, unlike the latter, the former is not a conventional dimensionless number since it is not the ratio of two competing forces. Nevertheless, the phase diagram indicates that both the dimensionless numbers N_b and N_f do, in fact, play the role of regime delimiters, with values of $N_f = 1$ and $N_b = 1$ roughly separating fracturing vs. non-fracturing for the former, and uniform invasion vs. viscous fingering and invasive fracturing vs. non-invasive fracturing for the latter. A new flow regime, mixing fracturing and fingering is found between the regions of non-invasive fracturing and viscous fingering, for $N_b > 1$ and a certain range of N_f. Interestingly, in the region $N_b > 1$, sufficiently large values of the fracturing number effectively prohibits viscous fingering, apparently favoring flow within the fractures over porous invasion. Finally, the red rectangle shown in Fig. 13 represents the region of the diagram explored by the experiments. The latter was obviously able to showcase the two regimes of invasive fracturing and uniform invasion, while our simulations indicate the possibility of three more regimes that are beyond the range of conditions studied experimentally.

For practical purposes, this phase diagram might provide insight on the type of flow regime that can be expected at the field scale. For instance, it is well known that viscous fingering decreases the efficiency of fluid–fluid displacement in industrial applications (e.g., enhanced oil recovery (Pinilla et al., 2021)). It is expected that industrial hydraulic fracturing may also suffer from this efficiency decrease. Indeed, our results suggest the existence of a flow regime combining hydraulic fracturing and viscous fingering, provided that the branching number N_b is sufficiently large. To estimate the latter, consider three types of field applications. First, in the context of oil recovery, if water ($\eta_w \sim 10^{-6}\,\text{kPa s}$) is used to displace oil ($\eta_o \sim 10^{-3}\,\text{kPa s}$), through a reservoir of permeability $k \sim 10^{-9}\,\text{mm}^2$, then $N_b \sim 10^{10}$. The injection borehole is assumed to have a radius of $l_0 \sim 100\,\text{mm}$. Second, in the context of CO_2

sequestration, where brine is displaced for water co-production, one can estimate $\mathrm{N}_b \sim 10^{12}$. The invading fluid, supercritical CO_2, is assumed to have a viscosity of 10^{-7} kPa s, whereas the defending fluid, brine, is assumed to have the same viscosity as water, and the permeability is the same as in the first application. Third, in the context of geothermal reinjection, even though the invading fluid, water, is the same as the defending fluid, the viscosity of the former can be lower than that of the latter when its temperature is larger (Mcdowell et al., 2016). As in Mcdowell et al. (2016), when the viscosity of the invading and defending fluid is 10^{-4} kPa s and 10^{-3} kPa s, respectively, and the permeability is 10^{-7} mm^2, then $\mathrm{N}_b \sim 10^{10}$. In all, the branching numbers for field applications are much larger than the range studied in Fig. 13, so that the type of flow cannot be ascertained for the moment. Note also that in real reservoirs, the flow regimes are not expected to be as distinguishable as in the simulations shown here. In particular, invasive fracturing, also called leak-off, can occur through existing natural cracks, even for tight geological formations (Chen et al., 2021). This means that invasive fracturing could occur for high values of N_b. Results that are perhaps more applicable to the kinds of porous media encountered in the field could be obtained by replacing the random initial porosity field by a more realistic one, for example, or by incorporating existing fracture networks.

5. Conclusion

In this work, a double phase-field approach regularizing both cracks and fluid–fluid interfaces is introduced. Derived within the frameworks of continuum thermodynamics and linear poroelasticity, the model behavior is characterized by a tight three-way coupling between multiphase fluid flow, poromechanics, and fracturing. Through finite-element discretization and numerical simulations, the model was validated against Hele–Shaw experiments, both directly and via the reconstruction of a phase diagram discriminating porous invasion from hydraulic fracturing. The parameter space was then explored beyond experimental capabilities to discover a variety of flow regimes, including a combination of fracturing and viscous fingering.

The model employs many simplifying assumptions that permit relatively low computational cost while satisfyingly reproducing relatively complex experiments. However, in future works, it will be of interest to explore the influence of higher-fidelity modeling choices. First, the small strain assumption underpinning linear poroelasticity is at the limit of validity in the present setting and may be replaced by finite-strain kinematics, as in Ehlers (2018) or Paulin et al. (2022). The model presented in this work was developed with a view towards subsurface engineering applications, in which the small strain assumption is often valid. Second, interpreting the packing of the experimental beads as a continuum is at the limit of validity as well. This could be addressed by resorting to explicitly modeling the microstructure on one hand or by experiments where the microstructural scale is much smaller than the domain size, on the other. Third, the binary fluid flow description can be enriched by replacing our Darcy–Poisseuille flow model by a Darcy–Stokes flow model, as introduced by Ehlers and Luo (2017), and Wilson and Landis (2016). Fourth, provided light modifications such as the introduction of a capillary pressure, our model can accommodate capillary flows in addition to viscous flows.

Ultimately, the model presented in this contribution could be used to predict and control the type of flows in field applications, as it bridges laboratory and field scales.

CRediT authorship contribution statement

Alexandre Guével: Methodology, Formal analysis, Investigation, Writing – original draft. **Yue Meng:** Writing–review. **Christian Peco:** Methodology, Writing–review. **Ruben Juanes:** Funding acquisition, Writing–review. **John E. Dolbow:** Funding acquisition, Supervision, Conceptualization, Writing – review & editing.

Declaration of competing interest

The authors declare that they have no known competing financial interests or personal relationships that could have appeared to influence the work reported in this paper.

Data availability

Data will be made available on request.

Acknowledgments

This work was the result of a collaboration between researchers at Duke and MIT, largely supported by a set of collaborative National Science Foundation research grants, in particular National Science Foundation grant CMMI-1933367 to Duke University, National Science Foundation grant CMMI-1933416 to MIT, and National Science Foundation grant CMMI-1826221 to Penn State. The support is gratefully acknowledged. Any opinions, findings, and conclusions or recommendations expressed in this material are those of the authors and do not necessarily reflect the views of the National Science Foundation.

Table B.1
Summary of the values chosen for the different model parameters.

Name	Symbol	Unit	Exp. value	Num. value
height of Hele–Shaw cell	H	mm	1.96	/
outer radius of Hele–Shaw cell	r_o	mm	53	53
beads diameter	d	mm	2	/
packing fraction	$1-\phi_0$	–	0.60	0.60
cement volume ratio	C	%	$[0,3]$	/
oil viscosity	η_o	kPa s	$[0.029, 0.29]$	$[10^{-4}, 1]$
water viscosity	η_w	kPa s	10^{-6}	$[10^{-6}, 10^{-3}]$
permeability	k	mm^2	$[(0.02d)^2, (0.06d)^2]$	/
permeability coeff	$\bar{k}$	mm^2	/	$[10^{-4}, 10^{-1}]$
surface tension	γ	kPa mm	0.03	0.03
Young's modulus of granular pack	E	kPa	331	331
drained bulk modulus of granular pack	K	kPa	184	184
Poisson ratio of granular pack	ν	kPa	0.2	0.2
bulk modulus of solid grains	K_s	kPa	1600	1600
nucleation energy	ψ_c	kPa	/	$0.0015C^2$
fracture toughness	G_c	kPa mm	$(0.26C+1.00)^2$	$(0.26C+1.00)^2$
damage viscosity	β	kPa s	/	$65.7\sqrt{C}$
regularization length for S	l_S	mm	/	4.0
regularization length for d	l_d	mm	/	4.0
Inner boundary condition for $\boldsymbol{w}_w$	w_i	mm/s	/	50
Inner boundary condition for μ	μ_i	kPa	/	0.006
Outer boundary condition for μ	μ_o	kPa	/	0.02

Appendix A. Derivation of the equivalent forms of the solid mass balance

In this appendix, the equivalent forms of the solid mass balance (5) are derived, following Borja's derivation (Borja, 2006). The assumed constitutive dependency of the partial solid density $\rho_s = \hat{\rho}_s(p)$ yields

$$\begin{aligned}\dot{\rho}_s &= \hat{\rho}_s'(p)\dot{p}\\ &= \dot{p}/K_s,\end{aligned} \tag{A.1}$$

where the matrix bulk modulus $K_s = \rho_s/\hat{\rho}_s'(p)$ is introduced, and the prime denotes the ordinary derivative.

The left-hand side of the solid mass balance $(4)_1$ then becomes:

$$\begin{aligned}\dot{\rho}^s + \rho^s\nabla\cdot\boldsymbol{v}_s &= \dot{\overline{1-\phi}}\rho_s + (1-\phi)\dot{\rho}_s + (1-\phi)\rho_s\nabla\cdot\boldsymbol{v}_s\\ &= \dot{\overline{1-\phi}}\rho_s + (1-\phi)\rho_s\dot{p}/K_s + (1-\phi)\rho_s\nabla\cdot\boldsymbol{v}_s,\end{aligned} \tag{A.2}$$

which provides, upon dividing by ρ_s, the result $(5)_1$.

For the second form $(5)_2$, the second constitutive dependency $p = \hat{p}(\phi, \rho^s)$ is employed, which yields:

$$\dot{p} = \frac{\partial\hat{p}}{\partial\phi}\dot{\phi} + \frac{\partial\hat{p}}{\partial\rho^s}\dot{\rho}^s. \tag{A.3}$$

Due to $(5)_1$ and $(4)_1$, and gathering the terms in $\dot{p}$ and $\nabla\cdot\boldsymbol{v}_s$, this becomes:

$$\left(1 - \frac{1-\phi}{K_s}\frac{\partial\hat{p}}{\partial\phi}\right)\dot{p} = -\left(-(1-\phi)\frac{\partial\hat{p}}{\partial\phi} + \rho^s\frac{\partial\hat{p}}{\partial\rho^s}\right)\nabla\cdot\boldsymbol{v}_s. \tag{A.4}$$

Upon introducing the skeleton bulk modulus

$$K = (1-\phi)\left(-(1-\phi)\frac{\partial\hat{p}}{\partial\phi} + \rho^s\frac{\partial\hat{p}}{\partial\rho^s}\right)\Big/\left(1 - \frac{1-\phi}{K_s}\frac{\partial\hat{p}}{\partial\phi}\right), \tag{A.5}$$

(A.4) becomes:

$$(1-\phi)\dot{p} = -K\nabla\cdot\boldsymbol{v}_s. \tag{A.6}$$

Finally, the second result $(5)_2$ is recovered by combining (5) and $(A.6)_1$, and introducing the Biot coefficient:

$$b = 1 - K/K_s. \tag{A.7}$$

Appendix B. Summary table of the experiment's and model's parameters

See Table B.1

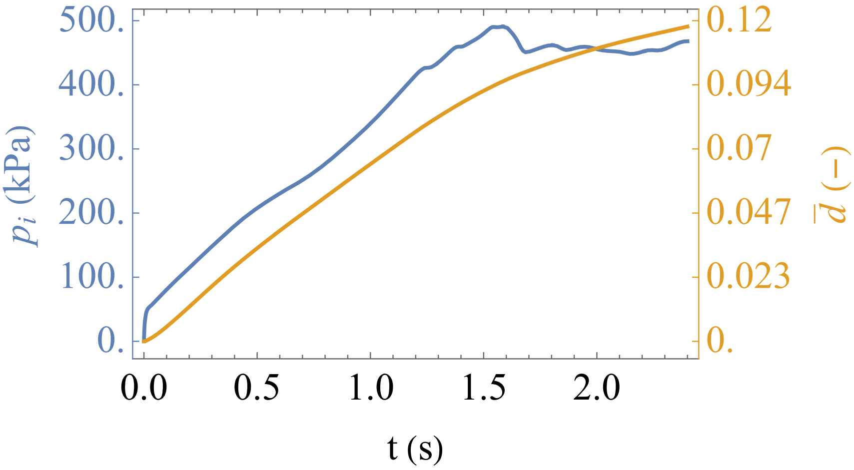

Fig. C.14. Comparison of the injection pressure curve with the average damage curve in the simulation reproducing the experiment.

Appendix C. Comparison injection pressure and average damage

See Fig. C.14

References

Abels, H., Garcke, H., Grün, G., 2012. Thermodynamically consistent, frame indifferent diffuse interface models for incompressible two-phase flows with different densities. Math. Models Methods Appl. Sci. 22 (03), 1150013.
Anderson, D.M., McFadden, G.B., Wheeler, A.A., 1998. Diffuse-interface methods in fluid mechanics. Annu. Rev. Fluid Mech. 30 (1), 139–165.
Biot, M.A., 1941. General theory of three-dimensional consolidation. J. Appl. Phys. 12 (2), 155–164.
Borja, R.I., 2006. On the mechanical energy and effective stress in saturated and unsaturated porous continua. Int. J. Solids Struct. 43, 1764–1786.
Bourdin, B., Francfort, G., Marigo, J., 2000. Numerical experiments in revisited brittle fracture. J. Mech. Phys. Solids 48, 797–826.
Bowen, R.M., 1976. Part I - Theory of mixtures. In: Eringen, A.C. (Ed.), Continuum Physics. Academic Press, ISBN: 978-0-12-240803-8, pp. 1–127. http://dx.doi.org/10.1016/B978-0-12-240803-8.50017-7.
Bowen, R.M., 1980. Incompressible porous media models by use of the theory of mixtures. Internat. J. Engrg. Sci. 18 (9), 1129–1148.
Cahn, J.W., Hilliard, J.E., 1958. Free energy of a nonuniform system. I. Interfacial free energy. J. Chem. Phys. 28 (2), 258–267.
Carrillo, F.J., Bourg, I.C., 2021. Modeling multiphase flow within and around deformable porous materials: a Darcy-Brinkman-Biot approach. Water Resour. Res. 57 (2), e2020WR028734.
Chen, B., Barboza, B.R., Sun, Y., Bai, J., Thomas, H.R., Dutko, M., Cottrell, M., Li, C., 2021. A review of hydraulic fracturing simulation. Arch. Comput. Methods Eng. 1–58.
Cogswell, D.A., Szulczewski, M.L., 2017. Simulation of incompressible two-phase flow in porous media with large timesteps. J. Comput. Phys. 345, 856–865.
Coleman, B.D., Noll, W., 1963. The thermodynamics of elastic materials with heat conduction and viscosity. Arch. Ration. Mech. Anal. 13 (1), 167–178. http://dx.doi.org/10.1007/bf01262690.
Coussy, O., 2004. Poromechanics. John Wiley & Sons.
Cueto-Felgueroso, L., Juanes, R., 2008. Nonlocal interface dynamics and pattern formation in gravity-driven unsaturated flow through porous media. Phys. Rev. Lett. 101 (24), 244504.
Cueto-Felgueroso, L., Juanes, R., 2009. A phase field model of unsaturated flow. Water Resour. Res. 45 (10).
Cueto-Felgueroso, L., Juanes, R., 2014. A phase-field model of two-phase Hele–Shaw flow. J. Fluid Mech. 758, 522–552.
da Silva, Jr., M.N., Duda, F.P., Fried, E., 2013. Sharp-crack limit of a phase-field model for brittle fracture. J. Mech. Phys. Solids 61 (11), 2178–2195.
De Boer, R., 2012. Theory of Porous Media: Highlights in Historical Development and Current State. Springer Science & Business Media.
Dede, L., Garcke, H., Lam, K.F., 2018. A Hele–Shaw–Cahn–Hilliard model for incompressible two-phase flows with different densities. J. Math. Fluid Mech. 20 (2), 531–567.
Dong, S., 2014. An outflow boundary condition and algorithm for incompressible two-phase flows with phase field approach. J. Comput. Phys. (ISSN: 0021-9991) 266, 47–73. http://dx.doi.org/10.1016/j.jcp.2014.02.011.
Ehlers, W., 2002. Foundations of multiphasic and porous materials. In: Porous Media. Springer, pp. 3–86.
Ehlers, W., 2018. Effective stresses in multiphasic porous media: a thermodynamic investigation of a fully non-linear model with compressible and incompressible constituents. Geomech. Energy Environ. 15, 35–46.
Ehlers, W., Luo, C., 2017. A phase-field approach embedded in the theory of porous media for the description of dynamic hydraulic fracturing. Comput. Methods Appl. Mech. Engrg. 315, 348–368.
Fourar, M., Lenormand, R., 1998. A viscous coupling model for relative permeabilities in fractures. In: Spe Annual Technical Conference and Exhibition. OnePetro.
Francfort, G.A., Marigo, J.-J., 1998. Revisiting brittle fracture as an energy minimization problem. J. Mech. Phys. Solids 46 (8), 1319–1342.
Fried, E., Gurtin, M.E., 1994. Dynamic solid-solid transitions with phase characterized by an order parameter. Physica D 72 (4), 287–308. http://dx.doi.org/10.1016/0167-2789(94)90234-8.
Geelen, R., Liu, Y., Hu, T., Tupek, M., Dolbow, J.E., 2019. A phase-field formulation for dynamic cohesive fracture. Comput. Methods Appl. Mech. Engrg.
Gurtin, M.E., 1996. Generalized Ginzburg–Landau and Cahn–Hilliard equations based on a microforce balance. Physica D 92, 178–192.
Gurtin, M.E., Fried, E., Anand, L., 2010. The Mechanics and Thermodynamics of Continua. Cambridge University Press.
Gurtin, M.E., Polignone, D.A., Viñals, J., 1995. Two-phase binary fluids and immiscible fluids described by an order parameter. Math. Models Methods Appl. Sci. 6, 815–831.

Heider, Y., 2021. A review on phase-field modeling of hydraulic fracturing. Eng. Fract. Mech. 253, 107881.

Heider, Y., Sun, W., 2020. A phase field framework for capillary-induced fracture in unsaturated porous media: Drying-induced vs. hydraulic cracking. Comput. Methods Appl. Mech. Engrg. 359, 112647.

Holtzman, R., Szulczewski, M.L., Juanes, R., 2012. Capillary fracturing in granular media. Phys. Rev. Lett. 108 (26), 264504.

Hu, T., Guilleminot, J., Dolbow, J.E., 2020. A phase-field model of fracture with frictionless contact and random fracture properties: Application to thin-film fracture and soil desiccation. Comput. Methods Appl. Mech. Engrg. 368, 113106.

Hu, T., Talamini, B., Stershic, A.J., Tupek, M., Dolbow, J.E., 2021. A variational phase-field model for ductile fracture with coalescence dissipation. Comput. Mech. 1–25.

Juanes, R., Meng, Y., Primkulov, B.K., 2020. Multiphase flow and granular mechanics. Phys. Rev. Fluids 5, 110516.

Kim, J., 2012. Phase-field models for multi-component fluid flows. Commun. Comput. Phys. 12 (3), 613–661.

Lee, H.-G., Lowengrub, J., Goodman, J., 2002. Modeling pinchoff and reconnection in a Hele–Shaw cell. I. The models and their calibration. Phys. Fluids 14 (2), 492–513.

Lee, S., Mikelic, A., Wheeler, M.F., Wick, T., 2018. Phase-field modeling of two phase fluid filled fractures in a poroelastic medium. Multiscale Model. Simul. 16 (4), 1542–1580.

Lenormand, R., Touboul, E., Zarcone, C., 1988. Numerical models and experiments on immiscible displacements in porous media. J. Fluid Mech. 189, 165–187.

Li, W., Meng, Y., Primkulov, B.K., Juanes, R., 2021. Photoporomechanics: an experimental method to visualize the effective stress field in fluid-filled granular media. Phys. Rev. A 16 (2), 024043.

Lowengrub, J., Truskinovsky, L., 1998. Quasi-incompressible Cahn–Hilliard fluids and topological transitions. Proc. R. Soc. Lond. Ser. A Math. Phys. Eng. Sci. 454 (1978), 2617–2654.

MacMinn, C.W., Dufresne, E.R., Wettlaufer, J.S., 2016. Large deformations of a soft porous material. Phys. Rev. A 5 (4), 044020.

Marigo, J.-J., Maurini, C., Pham, K., 2016. An overview of the modelling of fracture by gradient damage models. Meccanica 51, 3107–3128.

Mcdowell, A., Zarrouk, S.J., Clarke, R., 2016. Modelling viscous fingering during reinjection in geothermal reservoirs. Geothermics (ISSN: 0375-6505) 64, 220–234. http://dx.doi.org/10.1016/j.geothermics.2016.06.003.

Meng, Y., Li, W., Juanes, R., 2022a. Fracturing in wet granular media illuminated by photoporomechanics. Phys. Rev. A 18 (6), 064081.

Meng, Y., Li, W., Juanes, R., 2022b. Personal communication.

Meng, Y., Li, W., Juanes, R., 2023. Crossover from viscous fingering to fracturing in cohesive wet granular media: a photoporomechanics study. Soft Matter http://dx.doi.org/10.1039/d3sm00897e, (in press).

Meng, Y., Primkulov, B.K., Yang, Z., Kwok, C.Y., Juanes, R., 2020. Jamming transition and emergence of fracturing in wet granular media. Phys. Rev. Res. 2 (2), 022012.

Miehe, C., Mauthe, S., 2016. Phase field modeling of fracture in multi-physics problems. Part III. crack driving forces in hydro-poro-elasticity and hydraulic fracturing of fluid-saturated porous media. Comput. Methods Appl. Mech. Engrg. (ISSN: 0045-7825) 304, 619–655. http://dx.doi.org/10.1016/j.cma.2015.09.021.

Miehe, C., Mauthe, S., Teichtmeister, S., 2015. Minimization principles for the coupled problem of Darcy–Biot-type fluid transport in porous media linked to phase field modeling of fracture. J. Mech. Phys. Solids (ISSN: 0022-5096) 82, 186–217. http://dx.doi.org/10.1016/j.jmps.2015.04.006.

Miehe, C., Welschinger, F., Hofacker, M., 2010. Thermodynamically consistent phase-field models of fracture: Variational principles and multi-field FE implementations. Internat. J. Numer. Methods Engrg. 83 (10), 1273–1311.

Papatzacos, P., 2002. Macroscopic two-phase flow in porous media assuming the diffuse-interface model at pore level. Transp. Porous Media 49 (2), 139–174.

Paulin, O.W., Morrow, L.C., Hennessy, M.G., MacMinn, C.W., 2022. Fluid–fluid phase separation in a soft porous medium. J. Mech. Phys. Solids 164, 104892.

Peco, C., Liu, Y., Rhea, C., Dolbow, J., 2019. Models and simulations of surfactant-driven fracture in particle rafts. Int. J. Solids Struct. (ISSN: 0020-7683) 156–157, 194–209. http://dx.doi.org/10.1016/j.ijsolstr.2018.08.014.

Permann, C.J., Gaston, D.R., Andrš, D., Carlsen, R.W., Kong, F., Lindsay, A.D., Miller, J.M., Peterson, J.W., Slaughter, A.E., Stogner, R.H., Martineau, R.C., 2020. MOOSE: Enabling massively parallel multiphysics simulation. SoftwareX (ISSN: 23527110) 11, 100430. http://dx.doi.org/10.1016/j.softx.2020.100430.

Pijaudier-Cabot, G., Bažant, Z.P., 1987. Nonlocal damage theory. J. Eng. Mech. 113 (10), 1512–1533.

Pinilla, A., Asuaje, M., Ratkovich, N., 2021. Experimental and computational advances on the study of Viscous Fingering: An umbrella review. Heliyon 7 (7), e07614.

Pyrak-Nolte, L.J., DePaolo, D.J., Pietraß, T., 2015. Controlling Subsurface Fractures and Fluid Flow: a Basic Research Agenda. Tech. Rep., USDOE Office of Science (SC)(United States).

Rehbinder, G., 1995. Analytical solutions of stationary coupled thermo-hydro-mechanical problems. Int. J. Rock Mech. Min. Sci. Geomech. Abstr. (ISSN: 0148-9062) 32 (5), 453–463. http://dx.doi.org/10.1016/0148-9062(95)00035-F.

Saffman, P.G., Taylor, G.I., 1958. The penetration of a fluid into a porous medium or Hele–Shaw cell containing a more viscous liquid. Proc. R. Soc. Lond. Ser. A Math. Phys. Eng. Sci. 245 (1242), 312–329.

Santillán, D., Juanes, R., Cueto-Felgueroso, L., 2018. Phase field model of hydraulic fracturing in poroelastic media: Fracture propagation, arrest, and branching under fluid injection and extraction. J. Geophys. Res. Solid Earth 123 (3), 2127–2155.

Truesdell, C., Toupin, R., 1960. The classical field theories. In: Principles of Classical Mechanics and Field Theory (Prinzipien der Klassischen Mechanik und Feldtheorie) Springer, pp. 226–858.

Wilson, Z.A., Landis, C.M., 2016. Phase-field modeling of hydraulic fracture. J. Mech. Phys. Solids 96, 264–290.

Zhao, B., MacMinn, C.W., Juanes, R., 2016. Wettability control on multiphase flow in patterned microfluidics. Proc. Natl. Acad. Sci. 113 (37), 10251–10256.

Zhou, J., Dong, Y., de Pater, C.J., Zitha, P.L., 2010. Experimental study of the impact of shear dilation and fracture behavior during polymer injection for heavy oil recovery in unconsolidated reservoirs. In: SPE Canada Unconventional Resources Conference, Vol. All Days. http://dx.doi.org/10.2118/137656-MS, SPE-137656-MS.